Research Article

Farhan Ali, Aurang Zaib, Umair Khan*, Muhammad Faizan Ahmed, Syed Sohaib Zafar, and Samia Elattar

Irreversibility analysis of a bioconvective two-phase nanofluid in a Maxwell (non-Newtonian) flow induced by a rotating disk with thermal radiation

https://doi.org/10.1515/phys-2025-0200
received December 12, 2024; accepted July 14, 2025

Abstract: This analysis examined the convective heat transport influence of stagnant point bioconvection movement of a Darcy–Forchheimer flow past a rotating disk with entropy generation analysis. The energy expression is contributed by the effect of thermal radiation and the heat generation/absorption rate. The second law analysis also accounted for the given study's inspection of the irreversible analysis. The Buongiorno nanoscale model simulates the Brownian movement and thermophoretic effect. Also, the Maxwell fluid model is used for non-Newtonian rheological characteristics, and a Darcy–Forchheimer flow model is used for the porous medium. The nonlinear model equations are transformed into dimensionless equations through an appropriate transformation. Further, the converted expressions were computed using the homotopic procedure. Moreover, the graphs illustrate the consequences of flow variables on microorganism profile density, concentration distributions, thermal, velocity, entropy, and the Bejan number. The inertia coefficient and non-Newtonian fluid variable reveal the significance of axial and radial velocity decrease. An enhancement in the thermal field is noted for the higher values of the radiation parameter and the Biot number. The larger magnitude of the Brinkman number escalates the rate of entropy and the Bejan number. The drag force decreased from 7.95 to 7.13% for the values of the inertia coefficient. Heat transport is enhanced by 22% as the larger magnitude of thermal radiation parameter (Rd) rises. Mass transfer is further enhanced by bioconvection, which increases nanoparticle dispersion by up to 18%.

Keywords: Maxwell fluid, nanofluid, Darcy-Forchheimer flow, rotating disk, thermal radiation

*** Corresponding author: Umair Khan,** Department of Mathematics, Saveetha School of Engineering, Saveetha Institute of Medical and Technical Sciences, Saveetha University, Chennai, 602105, Tamil Nadu, India; Department of Mathematics, Faculty of Science, Sakarya University, Serdivan/Sakarya, 54050, Turkey, e-mail: umairkhan@sakarya.edu.tr
Farhan Ali: Department of Mathematical Sciences, Federal Urdu University of Arts, Sciences & Technology, Gulshan-e-Iqbal, Karachi, 75300, Pakistan, e-mail: farhanali@fuuast.edu.pk
Aurang Zaib: Department of Mathematical Sciences, Federal Urdu University of Arts, Sciences & Technology, Gulshan-e-Iqbal, Karachi, 75300, Pakistan, e-mail: aurangzaib@fuuast.edu.pk
Muhammad Faizan Ahmed: Department of Mathematical Sciences, Federal Urdu University of Arts, Sciences & Technology, Gulshan-e-Iqbal, Karachi, 75300, Pakistan, e-mail: mfaizanahmed@fuuast.edu.pk
Syed Sohaib Zafar: Department of Mathematics and Sciences, Sir Syed University of Engineering and Technology, Karachi, Pakistan, e-mail: sohaib.zafar@ssuet.edu.pk
Samia Elattar: Department of Industrial and Systems Engineering, College of Engineering, Princess Nourah bint Abdulrahman University, P.O. Box 84428, Riyadh 11671, Saudi Arabia, e-mail: SAElattar@pnu.edu.sa

1 Introduction

Scientists have become increasingly interested in the non-Newtonian liquid flow due to their uses in industry and technological processes. Liquids exhibiting non-Newtonian behavior have numerous manufacturing purposes such as food making, optical fibers, polymer sheet production, printing, and hot rolling. Scientists and researchers focused their research on the non-Newtonian empirical fluid models. When shear stress is applied, they change the flow mechanism. In addition, fluid substances employed varying rheological characteristics for different non-Newtonian fluid models. In 1867, the Maxwell fluid [1] model was among the non-Newtonian fluids that described stress relaxation. Jawad *et al.* [2] explained the impact of second law analysis on Maxwell flow of nanofluid (NF) in the presence of magnetized effect for the Marangoni condition due to the stretching sheet. Ali *et al.* [3] explained the pressure gradient effect on the Maxwell convective flow of hybrid nanofluid (HNF) between two parallel

plates using an analytical method. Parvin *et al.* [4] illustrated the magnetization of the Maxwell two-phase NF subject to the Soret–Dufour impacts past a tilted surface and a shrinking surface. Safdar *et al.* [5] inspected the impact of the magneto-flow Maxwell nanomaterial considering the permeable medium in the presence of microorganisms. Algehyne *et al.* [6] analyzed the analytical Maxwell thermophysical properties of a hybrid NF due to a permeable vertical plate. Khan *et al.* [7] reported the effect of Darcian Forchheimer magneto-flow of Maxwell NF in the presence of Levenberg–Marquardt back-propagation. Jameel *et al.* [8] probed the irreversible process of Joule heating for the Maxwell NF with a double diffusion model due to a porous stretchable surface. Wang *et al.* [9] scrutinized the impact of three-dimensional melting heat transport on Maxwell NF through a porous sheet.

Uses for nanomaterials are diverse and include cooling structures [10], cancer medication, microelectronic air conditioning, industry cooling, scan identification, household appliances, the development of fresh energy sources, and a lot more. These days, it is very common to improve the innovative performance of solitary thermal systems to improve thermal transportation. Its impressive uses in the manufacturing of documents, healthcare devices, heat transfer systems, medications, heat transport, lubrication [11], microelectronics, and many other fields are the reason for this. The efficiency of heat transmission of ordinary liquids (water, engine oil, air, and ethylene glycols) can be improved using a variety of techniques. Enhancing the working materials' (base liquid's) heat conduction can also increase thermal transfer efficiency. By inserting nanoparticles, relying upon liquid thermal efficiency can be improved. Nanomaterials are particles with colloidal structures that persist in a base liquid at nanoscales (1–100 nm). The term "nanoparticle" was initially employed by Choi and Estman [12] to describe the improvement of base liquids' thermal conductivity. A revised model for improving the thermal transport of NFs is provided by Buongiorno [13]. Waqas *et al.* [14] discussed about the magneto flow of viscous NF in the presence of convective flow past a vertical sheet. Anjum *et al.* [15] described the impact of thermal analysis in the Eyring–Powell nanomaterial considering activation energy and microorganisms. Mabood *et al.* [16] discovered the radiative flow of micropolar two-phase nanomaterial using a semi-analytical technique. Ahmed *et al.* [17] explored the viscous flow in the nanomaterial subject to the irreversible process due to the stretchable sheet. Shahzad *et al.* [18] examined the non-Fourier heat flux on the micropolar nanomaterial in the presence of Darcy–Forchheimer flow between dual disks. Karthik *et al.* [19] investigated the role of thermophoretic particle deposition and ternary hybrid NFs past a movable sheet saturated in a porous medium. Elboughdiri *et al.* [20] inspected the unsteady stagnation point flow of motile microorganisms around a rotating sphere filled with ternary hybrid NFs and chemical reaction. Additional, research on different subject of the problem is emphasized by refs. [21–24].

The flow of fluids over a porous medium is widely used in scientific and ecological structures, including moving fluids in storage tanks, thermal power systems, catalysis, nuclear reactors, and oil spill drilling. The Darcy–Forchheimer warmed rule allows us to incorporate material with pores into the fluid region for dispersal. Porous media communication has substantial uses in heat exchange building design, geothermal energy, geophysical sciences, catalyst reactors, groundwater drainage systems, insulating technology, petroleum safety devices, and storage systems for energy. Darcy [25], a Frenchman, first proposed the concept of liquid flow across porous media in 1856. However, due to its limited permeability and reduced motion, this concept may not be widely adopted. Philipp Forchheimer [26] added a quadratic velocity element to his momentum formula, addressing the glaring shortcoming. Muskat [27] referred to this concept as the "Forchheimer term." Sahu *et al.* [28] studied the viscoelastic flow in the single wall carbon nanotube and multi wall carbon nanotube due to the shrinkable rotating disk, considering the Darcian Forchheimer flow. Nisha and De [29] used the activation energy with the Darcian Forchheimer flow on Sisko fluid past a porous stretchable cylinder. Ahmed and Tiamiyu [30] inspected the non-Newtonian Darcy–Forchheimer time-dependent flow due to the movable surface. Shah *et al.* [31] emphasized the magnetized micropolar Darcian Forchheimer flow of melting heat transport due to porous disk.

The flow of fluid through a revolving disk is a fascinating research topic because of its numerous outstanding uses, which include rotor-stator systems, growth of crystals, electrolytic structures, ethereal distribution, wrapping deposits on surfaces, viscometers, maritime circulations, and healthcare devices, among others. Kármán produced a significant effort in the flow of fluid exposed to a spinning disk [32]. Khan *et al.* [33] observed the impact of thermal radiation of viscous NF due to a revolving disk. Song *et al.* [34] noted the viscous flow of the NF subject to thermal radiation and the Darcian Forchheimer flow due to away from the disk. Bu *et al.* [35] probed the role of squeezing the flow of NF for the radiative flow of heat flux past a rotating disk. Ahmed *et al.* [36] used the numerical computation of the viscous flow with thermal analysis past a revolving body with nonlinear thermal radiative. Sharma *et al.* [37] examined the flow of HNF induced by the radiative flow due to a rotating disk with a suction/injection effect. During high operational temperatures, thermal radiation plays a crucial part that cannot be disregarded. Given that

numerous industrial procedures involve exceedingly high temperatures, radiation empathy is essential for designing an appropriate procedure. In addition, it is essential to many industrial processes, including ionized physics, engines with internal combustion, crystal manufacturing, furnace development, and spaceships. Gomathi and Poulomi [38] inspected the comparative analysis dual solution of two non-Newtonian fluids subject to thermal radiation and chemical reaction. Ahmed *et al.* [39] discovered the impact of radiative heat flux on the flow of viscoelastic fluid in the presence of an irreversible process. Owhaib *et al.* [40] revealed the study of the radiation heat flux of nanoparticles due to a rotating disk. Nadeem *et al.* [41] examined the Darcian Forchheimer flow of the second law analysis in the heat generation/absorption considering the thermal radiation. Sharma [42] developed the effect of Joule heating with a nonlinear thermal radiative ferrofluid of heat transportation due to a porosity disk. Most recently, Nasir *et al.* [43] reviewed the effect of Newtonian heating for the Maxwell nanomaterial for the nonlinear mixed convective and radiation heat flux with the first-order chemical reaction using a semi-analytical technique.

Currently, no work has studied the impact of the Maxwell bioconvection flow, radiative flux, second law analysis, and chemical reactions on NF flow from a porous rotating disk. This is the originality and the emphasis of the current work. The analysis takes into account Darcy–Forchheimer, the stagnation point flow, and heat generation/absorption effects. We use convective, thermal, and boundary conditions to comprehensively evaluate temperature distributions. Buongiorno's nanoscale model with two components is implemented. A first-order chemical reaction is examined. The flow model is created using nondimensional equations with relevant variables. The models are given using the convergence Liao [44] homotopic analysis method (HAM) through the Mathematica 12 program. Verification of HAM results using special cases from the published work is presented. The study visualizes and interprets the impact of various flow factors (*e.g.*, stretching variable, inertia coefficient, porosity variable, thermal radiation, chemical reaction parameter, Peclet number, and bioconvection Lewis number) on movement features. Included are convergence studies for HAM estimates. The outcomes are described as thermal processes in microchip technology, vehicles, and heat exchangers. The questions listed below will have the responses revealed to the existing study:

- How does the Darcy–Forchheimer equation affect the Maxwell NF?
- How does the stagnation point affect the velocity of the Maxwell NF by using the velocity ratio variable?
- What are the phenomena of Maxwell NF against various physical variables?
- What is the role of the Biot number on the rate of heat transfer?
- How does the skin friction coefficient behave against the stretching parameter?

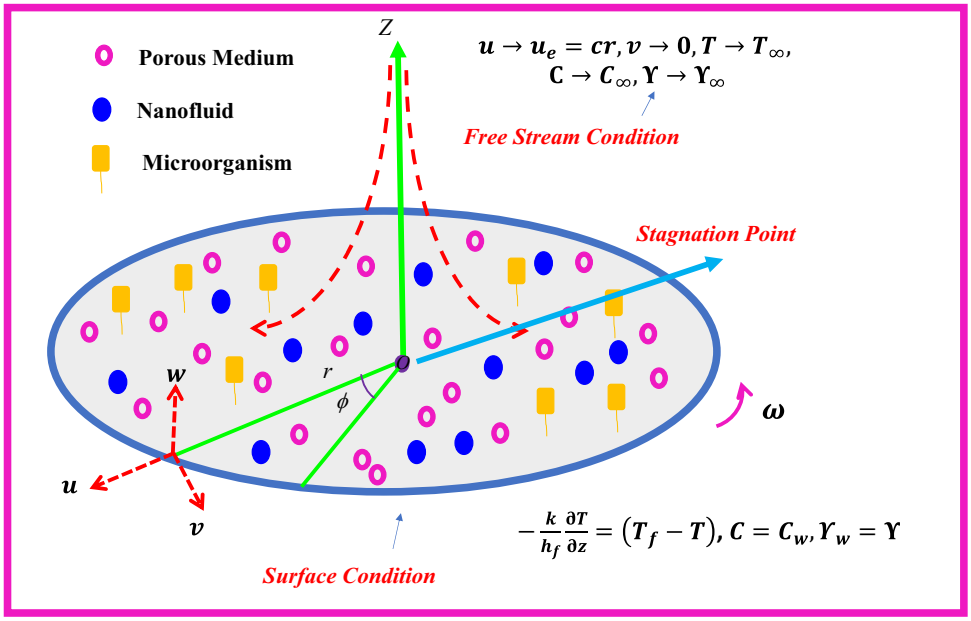

Figure 1: Geometry of the current flow problem.

2 Problem formulation

Let us assume the steady, axisymmetric flow of Maxwell nanoliquid across a permeable revolving disk. The flow is caused by the disk's rotation and radial stretching. The disk revolves through a uniform angular velocity ω and $z = 0$ as shown in Figure 1 [45]. The thermal radiation, bioconvection, convective boundary conditions, and chemical reactions are also scrutinized. The physical interpretation of the irreversibility analysis is also inspected. The constitutive equations are formulated through cylindrical coordinates (r, ϕ, z) with uniform velocity u, v, w. It is examined that $u_w = ar$ is the velocity of a stretchable rotating disk and $u_e = cr$ is the free stream velocity. T_f is the fluid temperature; T_w, C_W, and Y_w are the wall temperature, concentration, and microorganisms, respectively; T_∞ describes ambient temperature; C_∞ represents ambient concentration; and Y_∞ denotes the microorganisms.

The governing equations for the viscoelastic Maxwell fluid model can be described as follows:

$$\lambda_0 = -pI + B_1, \tag{1}$$

where λ_0 represents the time relaxation, B_1 represents the extra tensor, I represents a unit tensor, and p represents the pressure of the fluid. In addition,

$$B_1 + \beta_1(v.\,\nabla B_1 - LB_1 - B_1L^T) = \mu A_1, \tag{2}$$

$$\tau_0 = \nabla V, A_1 = L^{\mathrm{T}} + L, \tag{3}$$

where T describes the matrix transpose, L represents the velocity gradient, μ is the dynamics viscosity A_1 is the first Rivlin–Erikson tensor, and β_1 is a time relaxation parameter.

The governing equations are derived from the aforementioned assumptions [34,43]:

$$\frac{\partial u}{\partial r} + \frac{u}{r} + \frac{\partial w}{\partial z} = 0, \tag{4}$$

$$\begin{aligned} u\frac{\partial u}{\partial r} + w\frac{\partial u}{\partial z} - \frac{v^2}{r} + \beta_1\Bigg(u^2\frac{\partial^2 u}{\partial r^2} - \frac{2uv}{r}\frac{\partial v}{\partial r} + \frac{uv^2}{r^2} \\ + 2uw\frac{\partial^2 u}{\partial r\partial z} - \frac{2uv}{r}\frac{\partial v}{\partial z} + w^2\frac{\partial^2 u}{\partial z^2} + \frac{v^2}{r}\frac{\partial u}{\partial r}\Bigg) \\ = u_e\frac{\mathrm{d}u_e}{\mathrm{d}r} + \vartheta\frac{\partial^2 u}{\partial z^2} - F(u-u_e)^2 - \frac{\boldsymbol{\nu_f}}{K^*}(u-u_e), \end{aligned} \tag{5}$$

$$\begin{aligned} u\frac{\partial v}{\partial r} + w\frac{\partial v}{\partial z} + \frac{uv}{r} \\ + \beta_1\begin{pmatrix} u^2\frac{\partial^2 v}{\partial r^2} + \frac{2uv}{r}\frac{\partial u}{\partial r} - \frac{2u^2v}{r^2} + 2uw\frac{\partial^2 v}{\partial r\partial z} \\ - \frac{v^3}{r^2} + \frac{2vw}{r}\frac{\partial u}{\partial z} + \frac{v^2}{r}\frac{\partial v}{\partial r} + w^2\frac{\partial^2 v}{\partial z^2} \end{pmatrix}, \\ = \vartheta\frac{\partial^2 v}{\partial z^2} - \frac{\boldsymbol{\nu_f}}{K^*}v - Fv^2 \end{aligned} \tag{6}$$

$$\begin{aligned} u\frac{\partial T}{\partial r} + w\frac{\partial T}{\partial z} = \left(\alpha_f + \frac{16\sigma^* T_\infty^3}{3k\ (\rho C_p)_f}\right)\left[\frac{\partial^2 T}{\partial r^2} + \frac{1}{r}\frac{\partial T}{\partial r} + \frac{\partial^2 T}{\partial z^2}\right] \\ + \tau\Bigg\{D_B\left[\frac{\partial T}{\partial r}\frac{\partial C}{\partial r} + \frac{\partial T}{\partial z}\frac{\partial C}{\partial z}\right] \\ + \frac{D_B}{T_\infty}\left[\frac{\partial T}{\partial r} + \frac{\partial T}{\partial z}\right]^2\Bigg\} + \frac{Q_0}{(\rho C_p)_f}(T - T_\infty), \end{aligned} \tag{7}$$

$$\begin{aligned} u\frac{\partial C}{\partial r} + w\frac{\partial C}{\partial z} = D_B\left[\frac{\partial^2 C}{\partial r^2} + \frac{1}{r}\frac{\partial C}{\partial r} + \frac{\partial^2 C}{\partial z^2}\right] \\ + \left(\frac{D_T}{T_\infty}\right)\left[\frac{\partial^2 T}{\partial r^2} + \frac{1}{r}\frac{\partial T}{\partial r} + \frac{\partial^2 T}{\partial z^2}\right], \\ - \mathrm{Kr}(C - C_\infty) \end{aligned} \tag{8}$$

$$u\frac{\partial Y}{\partial r} + w\frac{\partial Y}{\partial z} + b\frac{W_c}{(C_w - C_\infty)}\frac{\partial}{\partial z}\left(Y\frac{\partial Y}{\partial z}\right) = D_m\frac{\partial^2 Y}{\partial z^2}, \tag{9}$$

where μ_f is the dynamic viscosity of the fluid, ν_f stands for the kinematic viscosity, F is the inertia coefficient, β_1 represents time for the fluid to relaxation time, T represents the temperature of a fluid, C is the concentration, D_B is the measure of Brownian motion, Kr is the rate of reaction, C_ρ is the heat capacity, α_f is the thermal diffusivity, D_T is the thermophoresis factor, k^* is the mean absorption term, ρ_f is the density, σ^* is the Stefan–Boltzmann coefficient, W_c is the swimming speed, k is the heat conductivity, the D_m is the microorganism diffusion.

The physical boundary conditions for the given model are as follows [36]:

$$\left.\begin{aligned} \frac{u}{r} = a, \quad w = 0, v = \omega r, \quad -\frac{k}{h_f}\frac{\partial T}{\partial z} = (T_f - T), \\ C = C_w, Y_w = \mathrm{Y}, \text{at } z = 0 \\ u \to u_e = cr, v \to 0, T \to T_\infty, \mathrm{C} \to C_\infty, Y \to Y_\infty \text{ as } z \to \infty. \end{aligned}\right\} \tag{10}$$

Furthermore, to ease the analysis of the given model, the following transformations are introduced [43]:

$$\left.\begin{aligned} u = r\omega F'(\zeta), \quad v = r\omega G(\zeta), \quad w = -2\sqrt{\omega\nu}F(\zeta), \\ \zeta = z\sqrt{\frac{\omega}{\nu}}, \quad \Theta(\zeta) = \frac{\mathrm{T} - \mathrm{T}_\infty}{T_f - \mathrm{T}_\infty}, \quad \Xi(\zeta) = \frac{\mathrm{C} - \mathrm{C}_\infty}{C_w - \mathrm{C}_\infty}, \\ \psi(\zeta) = \frac{Y - Y_\infty}{Y_w - Y_\infty}. \end{aligned}\right\} \tag{11}$$

By using Eq. (11), the constitutive Eqs. (4)–(9) are reduced to the following form of ordinary differential equations (ODEs)s:

$$\begin{aligned} F''' - 4\varepsilon[F^2F''' - FF'F'' - GF'F] - [(F')^2 - 2FF'' - G^2] \\ - \beta(F' - \lambda) - Fr(-\lambda^2 + (F')^2) = 0, \end{aligned} \tag{12}$$

$$\begin{aligned} G'' - 4\varepsilon[F^2G'' - FF'G' - FG''G] - 2[F'G - FG'] - \beta G \\ - \mathrm{Fr}G^2 = 0, \end{aligned} \tag{13}$$

$$\Theta''\left(1+\frac{4}{3}\mathrm{Rd}\right)+\mathrm{Pr}Q\Theta+\mathrm{Pr}F\Theta'+\mathrm{PrNb}\Xi'\Theta'+\mathrm{Pr\,Nt}(\Theta')^2=0, \tag{14}$$

$$\Xi''+\mathrm{Sc}F\Xi'+\frac{\mathrm{Nt}}{\mathrm{Nb}}\Theta''-\mathrm{Sc\,Cr}\Xi=0, \tag{15}$$

$$\psi''+\mathrm{Lb}F\psi'-\mathrm{Pe}[\psi'\Xi'+\Xi''(\psi+\varpi)]=0. \tag{16}$$

The boundary conditions are as follows:

$$\left.\begin{aligned}&F(0)=0,\quad F'(0)=\gamma,\quad G(0)=1,\\&\Theta'(0)=-\mathrm{Bi}(1-\Theta(0)),\Xi(0)=1,\psi(0)=1\\&F'(\infty)\to\lambda,G(\infty)\to0,\Theta(\infty)\to0,\Xi(\infty)\to0,\\&\psi(\infty)\to0.\end{aligned}\right\} \tag{17}$$

Here, the Deborah number is $\varepsilon=\beta_1\omega$, the porosity parameter is $\beta=\omega\frac{\nu_\mathrm{f}}{K^*}$, the inertia coefficient is $\mathrm{Fr}=\frac{C_\mathrm{b}}{K^{*1/2}}$, the radiation parameter is $\mathrm{Rd}=\frac{4\sigma^*T_\infty^3}{k_\mathrm{f}k^*}$, stretching parameter is $\gamma=\frac{a}{\omega}$, velocity ratio parameter is $\lambda=\frac{c}{\omega}$, the Prandtl number is $\mathrm{Pr}=\frac{\nu_\mathrm{f}}{\alpha_\mathrm{f}}$, the Brownian motion is $\mathrm{Nb}=\frac{\tau D_\mathrm{B}(c_\mathrm{w}-c_\infty)}{\nu_\mathrm{f}}$, heat source/sink heat source/sink is $Q=\frac{Q_0}{2\omega(\rho C_\mathrm{p})_\mathrm{f}}$, the thermophoresis parameter is $\mathrm{Nt}=\frac{\tau D_\mathrm{T}(T_\mathrm{f}-T_\infty)}{T_\infty\nu_\mathrm{f}}$, the Scimdth number is $\mathrm{Sc}=\frac{\nu_\mathrm{f}}{D_\mathrm{B}}$, the Biot number is $\mathrm{Bi}=\frac{h}{k}\sqrt{\frac{\nu_\mathrm{f}}{2\omega}}$, the Peclet number is $\mathrm{Pe}=\frac{bw_\mathrm{c}}{D_\mathrm{m}}$, the concentration of microorganisms $\varpi=\frac{Y_\infty}{Y_\mathrm{w}-Y_\infty}$, and the bioconvection Lewis number is $\mathrm{Lb}=\frac{\nu_\mathrm{f}}{D_\mathrm{m}}$.

2.1 Engineering quantities

The radial and tangential shear stress is denoted as τ_r and τ_θ, which are defined as follows:

$$C_\mathrm{f}=\frac{\tau|_{z=0}}{\rho_\mathrm{f}(r\omega)^2},$$

$$\left.\begin{aligned}\tau_\mathrm{r}&=\mu_\mathrm{f}\left(\frac{\partial u}{\partial z}\right)_{z=0}=r\omega\mu_\mathrm{f}\sqrt{\frac{2\omega}{\nu_\mathrm{f}}}F''(0),\\\tau_\theta&=\mu_\mathrm{f}\left(\frac{\partial v}{\partial z}\right)_{z=0}=r\omega\mu_\mathrm{f}\sqrt{\frac{2\omega}{\nu_\mathrm{f}}}G'(0)\end{aligned}\right\}. \tag{18}$$

The reduced form of friction factor is given as follows:

$$C_\mathrm{f}=\frac{\sqrt{\tau_\mathrm{r}^2+\tau_\theta^2}}{\rho_\mathrm{f}(r\omega)^2}=\frac{1}{\mathrm{Re}}[F''(0)^2+G'(0)^2]^{1/2}. \tag{19}$$

Also, $\mathrm{Nu_r}$, $\mathrm{Sh_r}$, and Nh are described as given as follows:

$$\mathrm{Nu_r}=\frac{rq_\mathrm{w}}{k(T_\mathrm{f}-T_\infty)},\ \mathrm{Sh_r}=\frac{rq_\mathrm{m}}{D_\mathrm{B}(C_\mathrm{w}-C_\infty)},\ \mathrm{Nh}=\frac{rq_\mathrm{n}}{D_\mathrm{m}(\mathrm{Y_w}-\mathrm{Y}_\infty)}, \tag{20}$$

where q_w,q_m, and q_n are given in the following form:

$$q_\mathrm{w}=-k\left(1+\frac{16\sigma^*T_\infty^3}{3k^*k}\right)\left(\frac{\partial T}{\partial z}\right)|_{z=0},\ q_m=-D_\mathrm{B}\frac{\partial C}{\partial z}|_{z=0},\ q_\mathrm{n}=-D_\mathrm{m}\frac{\partial \mathrm{Y}}{\partial z}|_{z=0}. \tag{21}$$

By using Eq. (11) in Eq. (20), we obtain the following equation:

$$\mathrm{Nu_r}=-\left(1+\frac{4}{3}\mathrm{Rd}\right)\Theta'(0),\quad \mathrm{Sh_r}=-\Xi'(0),\quad \mathrm{Nh_r}=-\psi'(0). \tag{22}$$

3 Analysis of entropy generation

The objective of this research is to analyze the rate of entropy creation in a volumetric system. Entropy generation is influenced by variables such as mass and thermal energy transfer irreversibility, as well as magnetic interaction irreversibility. The formula is as follows:

$$S_\mathrm{G}=\frac{k_\mathrm{f}}{T_\infty^2}\left(1+\frac{16\sigma^*T_\infty^3}{3k^*k_\mathrm{f}}\right)\left(\frac{\partial T}{\partial z}\right)^2+\frac{\mu}{T_\infty}\left(\left(\frac{\partial v}{\partial z}\right)^2+\left(\frac{\partial u}{\partial z}\right)^2\right)+\frac{\mu}{T_\infty K^*}(u^2+v^2)+\frac{R_\mathrm{D}}{C_\infty}\left(\frac{\partial C}{\partial z}\right)^2+\frac{R_\mathrm{D}}{\mathrm{Y}_\infty}\left(\frac{\partial \mathrm{Y}}{\partial z}\right)^2+\frac{R_\mathrm{D}}{T_\infty}\left(\frac{\partial T}{\partial z}\frac{\partial C}{\partial z}\right)+\frac{R_\mathrm{D}}{T_\infty}\left(\frac{\partial T}{\partial z}\frac{\partial \mathrm{Y}}{\partial z}\right). \tag{23}$$

The non-dimensional version of Eq. (20) is

$$\mathrm{Ns}(\zeta)=\Pi_1\left(1+\frac{4}{3}\mathrm{Rd}\right)\Xi'^2+\mathrm{Br}(F''^2+G'^2)+\mathrm{Br}\beta(F'^2+G^2)+\frac{\Pi_2}{\Pi_1}\mathrm{A_1}\Theta'^2+\frac{\Pi_3}{\Pi_1}\mathrm{A_2}\psi'^2+\mathrm{A_1}\Theta'\Xi'+\mathrm{A_2}\Theta'\psi'. \tag{24}$$

The ratio of heat and mass irreversibility to total irreversibility, mathematically:

$$\mathrm{Be}=\frac{\Pi_1\left(1+\frac{4}{3}\mathrm{Rd}\right)\Xi'^2+\frac{\Pi_2}{\Pi_1}A_1\Theta'^2+\frac{\Pi_3}{\Pi_1}A_2\psi'^2+A_1\Theta'\Xi'+A_2\Theta'\psi'}{\Pi_1\left(1+\frac{4}{3}\mathrm{Rd}\right)\Xi'^2+\mathrm{Br}(F''^2+\mathrm{G}'^2)+\mathrm{Br}\beta(\mathrm{F}'^2+\mathrm{G}^2)+\frac{\Pi_2}{\Pi_1}A_1\Theta'^2+\frac{\Pi_3}{\Pi_1}A_2\psi'^2+A_1\Theta'\Xi'+A_2\Theta'\psi'}. \tag{25}$$

In the aforementioned expression $\Pi_1 = \frac{(T_f - T_\infty)}{T_\infty}$ stands for temperature difference parameter, $\mathrm{Br} = \frac{\mu r^2 \omega^2}{k_f(T_f - T_\infty)}$ is the Brinkman number, $\Pi_2 = \frac{(C_W - C_\infty)}{C_\infty}$ expresses concentration difference parameter, $\Pi_3 = \frac{(Y_W - Y_\infty)}{Y_\infty}$ gives microorganism difference parameter, $A_1 = \frac{R_D(C_W - C_\infty)}{k_f}$ is the concentration diffusion parameter, and $A_2 = \frac{R_D(Y_W - Y_\infty)}{k_f}$ shows the microorganism diffusion parameter.

4 Solution of the homotopic procedure

The homotopic procedure tackles a general approach that applies to powerful and weak nonlinear expressions. The system is free of both small and significant constraints. The method described earlier is capable of helping solve all kinds of nonlinear partial differential equations (PDEs) that do not require splitting or linearization. This approach is linear and does not require a base function. The homotopic procedure method determines the solution of convergence and series systems.

Initial guesses are as follows:

$$\begin{aligned} &F_0(\zeta) = \lambda\zeta + (1-\lambda)(1-e^{-\zeta})\gamma, \quad G_0(\zeta) = e^{-\zeta}, \\ &\Theta_0(\zeta) = \frac{\mathrm{Bi}\cdot e^{-\zeta}}{1+\mathrm{Bi}}, \quad \Xi_0(\zeta) = e^{-\zeta}, \quad \psi_0(\zeta) = e^{-\zeta}, \end{aligned} \tag{26}$$

$$\begin{aligned} &\mathscr{L}(F) = F''' - F', \quad \mathscr{L}(G) = G'' - G, \\ &\mathscr{L}(\Theta) = \Theta'' - \Theta, \\ &\mathscr{L}(\Xi) = \Xi'' - \Xi, \quad \mathscr{L}(\psi) = \psi'' - \psi. \end{aligned} \tag{27}$$

Linear operator

$$\begin{aligned} &\mathscr{L}(F)(\wp_1 + \wp_2 e^{\zeta} + \wp_3 e^{-\zeta}) = 0, \\ &\mathscr{L}(G)(\wp_4 e^{\zeta} + \wp_5 e^{-\zeta}) = 0, \end{aligned} \tag{28}$$

$$\begin{aligned} &\mathscr{L}(\Theta)(\wp_6 e^{\zeta} + \wp_7 e^{-\zeta}) = 0, \\ &\mathscr{L}(\Xi)(\wp_8 e^{\zeta} + \wp_9 e^{-\zeta}) = 0, \\ &\mathscr{L}(\psi)(\wp_{10} e^{\zeta} + \wp_{11} e^{-\zeta}) = 0, \end{aligned} \tag{29}$$

where $\wp_i = 1 - 11$ coefficient constants.

4.1 Zero-order deformation

The zeroth-order deformation is created as follows:

$$(1-\mathscr{T})[F(\zeta,\mathscr{T}) - F_0(\zeta)] = \Im\hbar_F \aleph_F[F(\zeta,\mathscr{T}), G(\zeta,\mathscr{T})], \tag{30}$$

$$\begin{aligned} &(1-\mathscr{T})[G(\zeta,\mathscr{T}) - G_0(\zeta)] \\ &\quad = \Im\hbar_G \aleph_G[F(\zeta,\mathscr{T}), G(\zeta,\mathscr{T})], \end{aligned} \tag{31}$$

$$\begin{aligned} &(1-\mathscr{T})[\Theta(\zeta,\mathscr{T}) - \Theta_0(\zeta)] \\ &\quad = \Im\hbar_\Theta \aleph_\Theta[F(\zeta,\mathscr{T}), \Theta(\zeta,\mathscr{T}), \Xi(\zeta,\mathscr{T})], \end{aligned} \tag{32}$$

$$\begin{aligned} &(1-\mathscr{T})[\Xi(\zeta,\mathscr{T}) - \Xi_0(\vartheta)] \\ &\quad = \Im\hbar_\Xi \aleph_\Xi[F(\zeta,\mathscr{T}), \Theta(\zeta,\mathscr{T}), \Xi(\zeta,\mathscr{T})], \end{aligned} \tag{33}$$

$$\begin{aligned} &(1-\mathscr{T})[\psi(\zeta,\mathscr{T}) - \Gamma(\vartheta)] \\ &\quad = \Im\hbar_\psi \aleph_\psi[F(\zeta,\mathscr{T}), \Theta(\zeta,\mathscr{T}), \Xi(\zeta,\mathscr{T}), \psi(\zeta,\mathscr{T})]. \end{aligned} \tag{34}$$

Subject to the boundary conditions are as follows:

$$\begin{aligned} &F(0,\mathscr{T}) = 0, F'(0,\mathscr{T}) = 0, F(\infty,\mathscr{T}) = 0, \\ &G(0,\mathscr{T}) = 1, G(\infty,\mathscr{T}) = 0, \\ &\Theta(0,\mathscr{T}) = \mathrm{Bi}([\Theta(0,\mathscr{T}) - 1]), \Theta(\infty,\mathscr{T}) = 0, \Xi(0,\mathscr{T}) = 1, \\ &\Xi(\infty,\mathscr{T}) = 0, \psi(0,\mathscr{T}) = 1, \psi(\infty,\mathscr{T}) = 0. \end{aligned} \tag{35}$$

Nonlinear is described as $\aleph_F, \aleph_G, \aleph_\Theta, \aleph_\Xi$ and $\aleph_\psi$, and nonzero auxiliary variable is $\hbar_F, \hbar_G, \hbar_\Theta\ \hbar_\Xi$ and $\hbar_\psi$. Λ is an embedded parameter.

The nonlinear operator is elaborated as follows:

$$\begin{aligned} &\aleph_F[F(\zeta,\mathscr{T}), G(\zeta,\mathscr{T})] \\ &= \frac{\partial^3 F(\zeta,\mathscr{T})}{\partial\zeta^3} - (\beta)\frac{\partial F(\zeta,\mathscr{T})}{\partial\zeta} + \mathrm{Fr}\frac{\partial F(\zeta,\mathscr{T})}{\partial\zeta}\frac{\partial F(\zeta,\mathscr{T})}{\partial\zeta} \\ &\quad + \varepsilon(F\zeta,\mathscr{T})\frac{\partial^2 F(\zeta,\mathscr{T})}{\partial\zeta^2} - 4F^2(\zeta,\mathscr{T})\frac{\partial^3 F(\zeta,\mathscr{T})}{\partial\zeta^3} \\ &\quad - F(\zeta,\mathscr{T})\frac{\partial F(\zeta,\mathscr{T})}{\partial\zeta}\frac{\partial^2 F(\zeta,\mathscr{T})}{\partial\zeta^2}) - \frac{\partial F(\zeta,\mathscr{T})}{\partial\zeta}\frac{\partial F(\zeta,\mathscr{T})}{\partial\zeta} \\ &\quad + F(\zeta,\mathscr{T})\frac{\partial F(\zeta,\mathscr{T})}{\partial\zeta} + G^2(\zeta,\mathscr{T}), \end{aligned} \tag{36}$$

$$\begin{aligned} &\aleph_G[F(\zeta,\mathscr{T}), G(\zeta,\mathscr{T})] \\ &= \frac{\partial^2 G(\zeta,\mathscr{T})}{\partial\zeta^2} - 2\left(\frac{\partial G(\zeta,\mathscr{T})}{\partial\zeta}F(\zeta,\mathscr{T}) - \frac{\partial F(\zeta,\mathscr{T})}{\partial\zeta}G(\zeta,\mathscr{T})\right) \\ &\quad - (\beta)G(\zeta,\mathscr{T}) + \mathrm{Fr}G^2(\zeta,\mathscr{T}) - 4\varepsilon F^2(\zeta,\mathscr{T})\frac{\partial^2 G(\zeta,\mathscr{T})}{\partial\zeta^2} \\ &\quad + 4\varepsilon F(\zeta,\mathscr{T})\frac{\partial F(\zeta,\mathscr{T})}{\partial\zeta}\frac{\partial G(\zeta,\mathscr{T})}{\partial\zeta} \\ &\quad + 4\varepsilon F(\zeta,\mathscr{T})\frac{\partial^2 F(\zeta,\mathscr{T})}{\partial\zeta^2}G(\zeta,\mathscr{T}), \end{aligned} \tag{37}$$

$$\begin{aligned} &\aleph_\Theta[\Theta(\zeta,\mathscr{T}), \Xi(\zeta,\mathscr{T})] \\ &= \left(1 + \frac{4}{3}\mathrm{Rd}\right)\frac{\partial^2\Theta(\zeta,\mathscr{T})}{\partial\zeta^2} + \mathrm{Pr}\,\mathrm{Nb}\frac{\partial\Theta(\zeta,\mathscr{T})}{\partial\zeta}\frac{\partial\Xi(\zeta,\mathscr{T})}{\partial\zeta} \\ &\quad + \mathrm{Pr}\,\mathrm{Nt}\left(\frac{\partial\Theta(\zeta,\mathscr{T})}{\partial\zeta}\right)^2 + \mathrm{Pr}\,Q\Theta((\zeta,\mathscr{T})), \end{aligned} \tag{38}$$

$$\begin{aligned}\aleph_{\Xi}[\Theta(\zeta,\mathcal{T}),\Xi(\zeta,\mathcal{T})] &= \frac{\partial^2\Xi(\zeta,\mathcal{T})}{\partial\zeta^2} + \mathrm{Sc}\,F(\zeta,\mathcal{T})\frac{\partial\Xi(\zeta,\mathcal{T})}{\partial\zeta} \\ &\quad + \mathrm{Sc}\left(\frac{\mathrm{Nt}}{\mathrm{Nb}}\right)\frac{\partial^2\Theta(\zeta,\mathcal{T})}{\partial\zeta^2} - \mathrm{Cr}\,\Xi(\zeta,\mathcal{T}),\end{aligned} \tag{39}$$

$$\begin{aligned}\aleph_{\psi}[F(\zeta,\mathcal{T}),\Xi(\zeta,\mathcal{T}),\psi(\zeta,\mathcal{T})] &= \frac{\partial^2\psi(\zeta,\mathcal{T})}{\partial\zeta^2} + \mathrm{Lb}\,\mathrm{F}(\zeta,\mathcal{T})\frac{\partial\psi(\zeta,\mathcal{T})}{\partial\zeta} \\ &\quad - \mathrm{Pe}\left(\frac{\partial\psi(\zeta,\mathcal{T})}{\partial\zeta}\frac{\partial\Xi(\zeta,\mathcal{T})}{\partial\zeta}\right) \\ &\quad + \frac{\partial^2\Xi(\zeta,\mathcal{T})}{\partial\zeta^2}(\varpi+\psi(\zeta,\mathcal{T})),\end{aligned} \tag{40}$$

when $\mathcal{T}=0$, and $\mathcal{T}=1$ are given as follows:

$$F(\zeta;0)=F_0(\zeta),\ \Theta(\zeta;0)=\Theta_0(\zeta),\ \Xi(\zeta;0)=\Xi_0(\zeta),\ \psi(\zeta;0)=\psi_0(\zeta), \tag{41}$$

$$F(\zeta;1)=F_0(\zeta),\ \Theta(\zeta;1)=\Theta_0(\zeta),\ \Xi(\zeta;1)=\Xi_0(\zeta),\ \Gamma(\zeta;1)=\Gamma_0(\zeta). \tag{42}$$

If $\mathcal{T}$ is enhanced from 0 to 1, by the Tayalor expansion series:

$$F(\zeta,\mathcal{T})=F_0(\zeta)+\sum_{m=1}^{\infty}F_m(\zeta)\Lambda^m \Rightarrow F_m(\zeta) = \frac{1}{m!}\frac{\partial^m F(\zeta,\mathcal{T})}{\partial\zeta^m}\bigg|_{\mathcal{T}=0}, \tag{43}$$

$$G(\zeta,\mathcal{T})=G_0(\zeta)+\sum_{m=1}^{\infty}G_m(\zeta)\Lambda^m \Rightarrow G_m(\zeta) = \frac{1}{m!}\frac{\partial^m G(\zeta,\mathcal{T})}{\partial\zeta^m}\bigg|_{\mathcal{T}=0}, \tag{44}$$

$$\Theta(\zeta,\mathcal{T})=\Theta_0(\zeta)+\sum_{m=1}^{\infty}\Theta_m(\zeta)\Lambda^m \Rightarrow G_m(\zeta) = \frac{1}{m!}\frac{\partial^m \Theta(\zeta,\mathcal{T})}{\partial\zeta^m}\bigg|_{\mathcal{T}=0}, \tag{45}$$

$$\Xi(\zeta,\mathcal{T})=\Xi_0(\zeta)+\sum_{m=1}^{\infty}\Xi_m(\zeta)\Lambda^m \Rightarrow G_m(\zeta) = \frac{1}{m!}\frac{\partial^m \Xi(\zeta,\mathcal{T})}{\partial\zeta^m}\bigg|_{\mathcal{T}=0}, \tag{46}$$

$$\psi(\zeta,\mathcal{T})=\psi_0(\zeta)+\sum_{m=1}^{\infty}\psi_m(\zeta)\Lambda^m \Rightarrow \psi_m(\zeta) = \frac{1}{m!}\frac{\partial^m \psi(\zeta,\mathcal{T})}{\partial\zeta^m}\bigg|_{\mathcal{T}=0}. \tag{47}$$

4.2 The *m* order deformation

Using Eq. (33) for homotopy at m order, we obtain the following:

$$\mathcal{L}_{\mathrm{F}}[F_m(\zeta;\mathcal{T})-\mathcal{X}_m F_{m-1}(\zeta)] = \hbar_{\mathrm{F}}\mathcal{R}_{\mathrm{F},m}(\zeta), \tag{48}$$

$$\mathcal{L}_{\mathrm{G}}[G_m(\zeta;\mathcal{T})-\mathcal{X}_m G_{m-1}(\zeta)] = \hbar_{\mathrm{G}}\mathcal{R}_{\mathrm{G},m}(\zeta), \tag{49}$$

$$\mathcal{L}_{\Theta}[\Theta_m(\zeta;\mathcal{T})-\mathcal{X}_m \Theta_{m-1}(\zeta)] = \hbar_{\Theta}\mathcal{R}_{\Theta,m}(\zeta), \tag{50}$$

$$\mathcal{L}_{\Xi}[\Xi_m(\zeta;\mathcal{T})-\mathcal{X}_m \Xi_{m-1}(\zeta)] = \hbar_{\Xi}\mathcal{R}_{\Xi,m}(\zeta), \tag{51}$$

$$\mathcal{L}_{\psi}[\psi_m(\zeta;\mathcal{T})-\mathcal{X}_m \psi_{m-1}(\zeta)] = \hbar_{\psi}\mathcal{R}_{\psi,m}(\zeta), \tag{52}$$

with the mth-order boundary conditions:

$$\begin{aligned}\mathscr{R}_{\mathrm{F},m}(\zeta) &= F'''_{m-1} - \mathrm{Fr}\sum_{\ell=0}^{m-1}(-\lambda^2\mathscr{X}_m + F'_{m-1-\ell}F'_{m-1-\ell}) \\ &\quad - \beta(F'_{m-1-\ell} - \lambda\mathscr{X}_m) + 4\varepsilon F_{m-1-\ell}F_\ell F'''_{m-1} \\ &\quad + 4\varepsilon F'_{m-1-\ell}F''_a F_{m-1-\ell} + 4\varepsilon F'_{m-1-\ell}F_{m-1-\ell}G_\ell \\ &\quad - F_{m-1-\ell}F_\ell + 4G_\ell F'_\ell G_{m-1-\ell}G_\ell,\end{aligned} \tag{53}$$

$$\begin{aligned}\mathscr{R}_{\mathrm{G},m}(\zeta) &= G''_{m-1} - \mathrm{Fr}\sum_{\ell=0}^{m-1}G_{m-1}G_{m-1-\ell} - (\beta)G_{\ell-1+m} \\ &\quad + 4\varepsilon F_{m-1-\ell}F_\ell G'''_{m-1} + 4\varepsilon F'_{m-1-\ell}F_{m-1-\ell}G'_{m-1-\ell} \\ &\quad + 4\varepsilon F''_\ell G_{m-1-\ell}G_\ell - F_{m-1-\ell}F_\ell \\ &\quad - 2\sum_{a=0}^{m-1}G'_{m-1-\ell}F_{m-\ell} - F'_{m-1-\ell}G_\ell,\end{aligned} \tag{54}$$

$$\mathscr{R}_{\Theta,m}(\zeta) = \Theta''_{m-1} + \mathrm{Pr}\sum_{\ell=0}^{m-1}(F_{m-1-\ell}\Theta'_\ell - \mathrm{Nb}\,\mathrm{Nt}\Theta'_{m-1-\ell}\Xi'_\ell + \mathrm{Nt}\Theta'_{m-1-\ell}\Theta'_\ell + \Theta_{m-1}\quad Q), \tag{55}$$

$$\begin{aligned}\mathscr{R}_{\psi,m}(\zeta) &= \psi''_{m-1} + \mathrm{Lb}\sum_{\ell=0}^{m-1}(F_{m-1}\psi'_\ell) \\ &\quad - \mathrm{Pe}\sum_{\ell=0}^{m-1}(\psi'_{m-1-\ell}\Xi'_\ell + \Xi''_{m-1}(\varpi+\psi_{m-1-\ell})),\end{aligned} \tag{56}$$

and

$$\mathcal{X}_m = \left.\begin{matrix}0, m\le 1\\ 1, m>1\end{matrix}\right\}. \tag{57}$$

The solutions can be explained in general as follows:

$$\left.\begin{aligned}F_m - F_m^* &= \wp_1 + \wp_2 e^{\zeta} + \wp_3 e^{-\zeta}\\ G_m - G_m^* &= \wp_4 e^{\zeta} + \wp_5 e^{-\vartheta}\\ \Theta_m - \Theta_m^* &= \wp_6 e^{\vartheta} + \wp_7 e^{-\vartheta}\\ \Xi_m - \Xi_m^* &= \wp_8 e^{\vartheta} + \wp_9 e^{-\vartheta}\\ \Gamma_m - \Gamma_m^* &= \wp_{10} e^{\vartheta} + \wp_{11} e^{-\vartheta}\end{aligned}\right\}, \tag{58}$$

where F_m^*, G_m^*, Θ_m^*, Ξ_m^*, and ψ_m^* have a particular solution.

The average residual error for series solution of $F(\zeta)$, $G(\zeta)$, $\Theta(\zeta)$, $\Xi(\zeta)$, and $\psi(\zeta)$, nonzero auxiliary variables, is $\hbar_{\mathrm{F}}$, $\hbar_{\mathrm{G}}$, $\hbar_{\Theta}$ $\hbar_{\Xi}$, and $\hbar_{\psi}$. We use the average residual errors for the equation of the mth order as follows [40]:

$$\mathscr{H}_{\mathrm{F},m} = \frac{1}{\mathscr{N}} \times \sum_{e=0}^{j} \left[\mathscr{N}_{\mathrm{F}} \left(\sum_{l=0}^{k} F_i(e\Delta n), \sum_{l=0}^{k} G_i(e\Delta n), \sum_{l=0}^{k} \Theta_i(e\Delta n), \sum_{l=0}^{k} \Xi_i(e\Delta n), \sum_{l=0}^{k} \psi_i(e\Delta n) \right) \right]^2, \tag{59}$$

$$\mathscr{H}_{\mathrm{G},m} = \frac{1}{\mathscr{N}} \times \sum_{e=0}^{j} \left[\mathscr{N}_{\mathrm{F}} \left(\sum_{l=0}^{k} F_i(e\Delta n), \sum_{l=0}^{k} G_i(e\Delta n), \sum_{l=0}^{k} \Theta_i(e\Delta n), \sum_{l=0}^{k} \Xi_i(e\Delta n), \sum_{l=0}^{k} \psi_i(e\Delta n) \right) \right]^2, \tag{60}$$

$$\mathscr{H}_{\Theta,m} = \frac{1}{\mathscr{N}} \times \sum_{e=0}^{j} \left[\mathscr{N}_{\mathrm{F}} \left(\sum_{l=0}^{k} F_i(e\Delta n), \sum_{l=0}^{k} G_i(e\Delta n), \sum_{l=0}^{k} \Theta_i(e\Delta n), \sum_{l=0}^{k} \Xi_i(e\Delta n), \sum_{l=0}^{k} \psi_i(e\Delta n) \right) \right]^2, \tag{61}$$

$$\mathscr{H}_{\Xi,m} = \frac{1}{\mathscr{N}} \times \sum_{e=0}^{j} \left[\mathscr{N}_{\mathrm{F}} \left(\sum_{l=0}^{k} F_i(e\Delta n), \sum_{l=0}^{k} G_i(e\Delta n), \sum_{l=0}^{k} \Theta_i(e\Delta n), \sum_{l=0}^{k} \Xi_i(e\Delta n), \sum_{l=0}^{k} \psi_i(e\Delta n) \right) \right]^2, \tag{62}$$

$$\mathscr{H}_{\psi,m} = \frac{1}{\mathscr{N}} \times \sum_{e=0}^{j} \left[\mathscr{N}_{\mathrm{F}} \left(\sum_{l=0}^{k} F_i(e\Delta n), \sum_{l=0}^{k} G_i(e\Delta n), \sum_{l=0}^{k} \Theta_i(e\Delta n), \sum_{l=0}^{k} \Xi_i(e\Delta n), \sum_{l=0}^{k} \psi_i(e\Delta n) \right) \right]^2. \tag{63}$$

5 Numerical solution

The NDSolve approach is used to solve the system of Eqs. (12)–(16) with the boundary condition (17) to obtain the results. This technique uses numerical methods to solve differential equations. This method automatically discretizes the evaluation of data. This method attains exceptional precision and maintains a consistent level of stability. Furthermore, it achieves exceptional speed while utilizing little CPU resources and handling concise expressions.

5.1 Solution expression of homotopic convergence

The Homotopy analysis method has been used to compute the convergence analysis [44,46]. This approach requires an auxiliary variable, $\hbar$-curve. This allows us to alter the convergence region for $F''(0)$, $G'(0)$, $\Theta'(0)$, $\Xi'(0)$, and $\psi'(0)$. It is important to choose the right number for the auxiliary parameter $\hbar$ to control and speed up the convergence of the approximation series with the help of the so-called $\hbar$-curve. The 15th-order estimate gave us the $\hbar$-curve of $F''(0)$, $G'(0)$, $\Theta'(0)$, $\Xi'(0)$, and $\psi'(0)$. Figure 2(a) and (b) reveals that the range of region magnitude

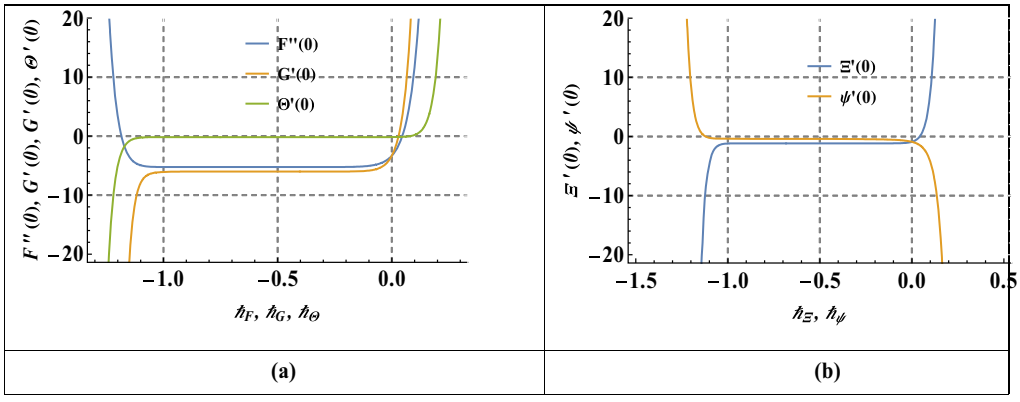

Figure 2: (a) $F''(0)$, $G(0)$, $\Theta'(0)$ for the $\hbar$-curve. (b) $\Xi'(0)$, $\psi(0)$ for the $\hbar$-curve.

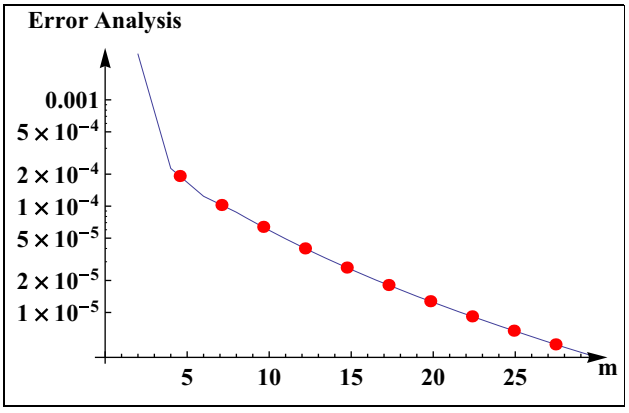

Figure 3: The total square residual error.

$-0.51 \le \hbar_F \le 0.11$, $-1.2 \le \hbar_G \le 0.12$ − $1.41 \le \hbar_\Theta \le 0.31$, $-1.4 \le \hbar_\Xi \le 0.12$, $-1.4 \le \hbar_\psi \le 0.1$. Figure 3 exhibited total square residual error. The 15th-order approximation results in the convergence of HAM as shown in Table 1. Table 2 reveals the total square residual error.

Figure 4(a)–(e) shows the comparison of numerical and analytical. Hence, we computed the 12th order of approximation for $F'(\zeta)$, $G(\zeta)$, $\Theta(\zeta)$, $\Xi(\zeta)$, and $\psi(\zeta)$.

6 Validation of the result

To confirm that the HAM estimations are accurate, several previous studies from the published literature are compared. As shown in Table 3, the contrasting findings of the skin friction coefficient in a limited situation are in excellent agreement with the literature. Thus, it is reasonable to say that there is a great deal of confidence in the current HAM solutions.

7 Results and discussion

The present part of this research displays visual information regarding velocity components, including radial $F(\zeta)$, azimuthal $G(\zeta)$, concentration field $\Xi(\zeta)$ and temperature profiles $\Theta(\zeta)$, entropy generation $\mathrm{Ns}(\zeta)$, and Bejan profile $\mathrm{Be}(\zeta)$, are shown in Figures 5–11. The physical outcome variables, such as the stretching variable (λ), rotating parameter (Υ), Deborah's number (ε), Porosity variable (β), inertia coefficient (Fr), Brownian motion (Nb), thermophoretic diffusion (Nt), Prandtl number (Pr), thermal radiation (Rd), heat source/sink (Q), chemical reaction variable

Table 1: Convergence analysis of HAM for $\beta = 0.1, \lambda = 0.1;\ \gamma = 0.4, \hbar_F = \hbar_G = \hbar_\Theta = \hbar_\Xi = \hbar_\psi = -0.56$, Bi = 0.2, Lb = 1.2, Nt = 0.2, ε = 0.5, Pe = 0.2, Pr = 0.9, Sc = 0.7, Cr = 1.0, $\varpi = 1.1$

M	$F''(0)$	$G(0)$	$\Xi'(0)$	$\Xi'(0)$	$\psi'(0)$
1	0.30000	1.32900	0.18027	1.13333	0.88256
5	0.36612	1.48196	0.18325	1.18026	0.62423
10	0.36890	1.49321	0.18130	1.27458	0.51302
15	0.36890	1.49321	0.18130	1.27458	0.51302
20	0.36890	1.49321	0.18130	1.27458	0.51302
25	0.36890	1.49321	0.18130	1.27458	0.51302
30	0.36890	1.49321	0.18130	1.27458	0.51302

Table 2: Average squared residual error is $\hbar_F = 0.36890$, $\hbar_G = 1.493210$, $\hbar_\Theta = 0.18130$, $\hbar_\Xi = 1.27458$, $\hbar_\psi = 0.51302$

m	$\mathcal{H}_{F,m}$	$\mathcal{H}_{G,m}$	$\mathcal{H}_{\Theta,m}$	$\mathcal{H}_{\Xi,m}$	$\mathcal{H}_{\psi,m}$
2	5.744725×10^{-4}	2.8732×10^{-4}	2.4976×10^{-4}	6.60017×10^{-4}	1.151505×10^{-3}
6	1.03188×10^{-6}	1.31933×10^{-6}	8.50479×10^{-4}	3.4779×10^{-6}	3.3132×10^{-4}
12	2.35733×10^{-9}	1.38214×10^{-8}	2.9881×10^{-4}	4.4029×10^{-7}	1.09597×10^{-4}
18	2.72019×10^{-11}	3.13983×10^{-10}	1.28763×10^{-4}	8.86161×10^{-8}	3.36798×10^{-6}
24	5.05576×10^{-13}	1.10736×10^{-11}	6.09797×10^{-6}	2.26792×10^{-8}	1.39112×10^{-6}
30	2.45552×10^{-13}	1.22731×10^{-11}	3.05375×10^{-6}	7.24909×10^{-9}	7.07786×10^{-7}

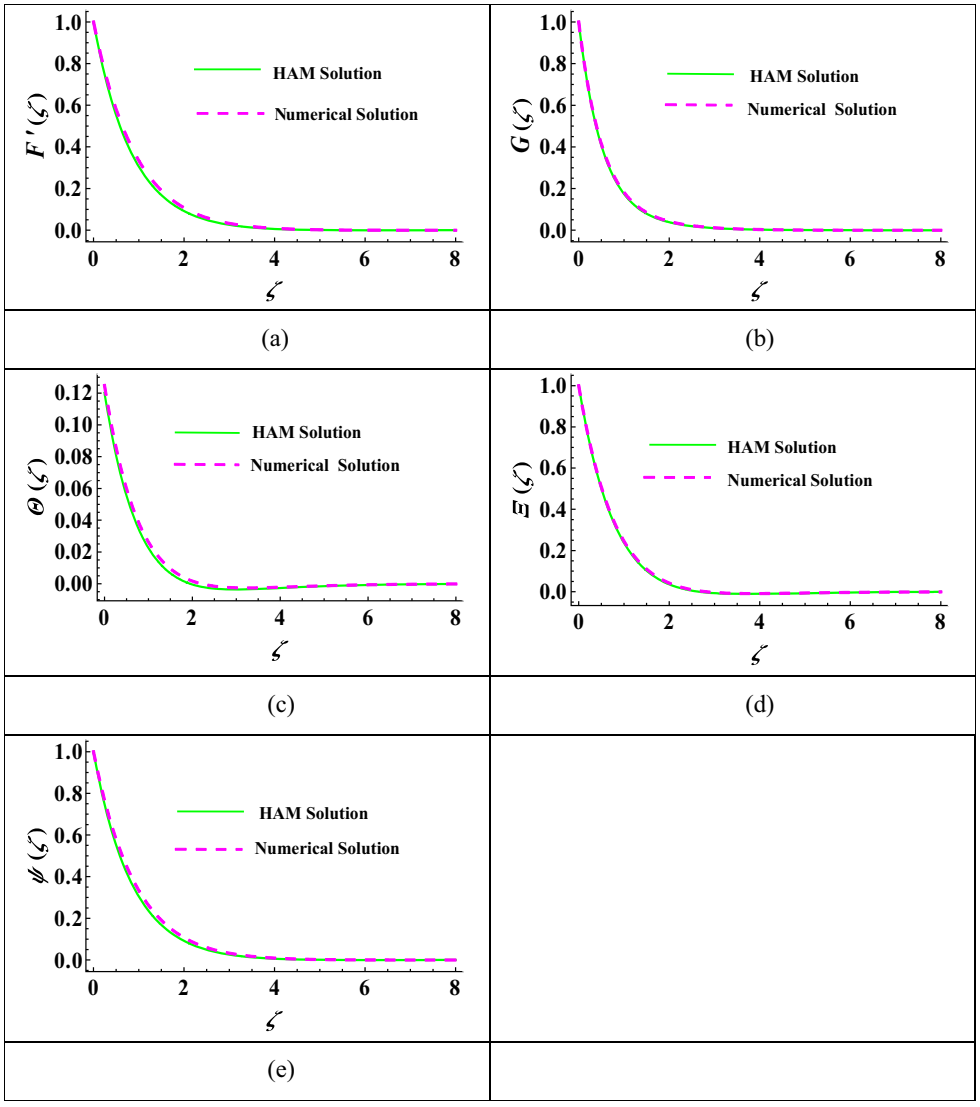

Figure 4: (a) Numerical and analytical comparison of $F'(\zeta)$. (b) Numerical and analytical comparison of $G(\zeta)$. (c) Numerically and analytically comparison of $\Theta(\zeta)$. (d) Numerically and analytically comparison of $\Xi(\zeta)$. (e) Numerical and analytical comparison of $\psi(\zeta)$.

Table 3: Comparison of λ with previously published results

λ	Ramesh *et al.* [47]	Mathew *et al.* [48]	Nisar *et al.* [43]	Current analysis (HAM analysis)
0.01	−0.9991	—	−0.99800	−0.99670
0.1	−0.9696	−0.9693	−0.96939	−0.96441
0.2	−0.9181	−0.91810	−0.91811	−0.91137
0.5	−0.6672	−0.66726	−0.66726	−0.66091
0.7	—	−0.43475	−0.43347	−0.431309
0.8	—	−0.29938	−0.29938	−0.29783
0.9	—	−0.15471	−0.15471	−0.15390
1.0	—	0	0	0

(Cr), Peclet number (Pe), Bioconvection Lewis number (Lb), temperature difference variable (Π_1), concentration difference variable (Π_2), microorganism difference variable (Π_3), concentration diffusion variable (A_1), and microorganism diffusion variable (A_2).

The influence of inertia coefficient (Fr), porosity variable (β), Deborah number (ε), and velocity ratio (λ) over radial velocity $F(\zeta)$ is shown in Figure 5(a)–(d). Figure 5(a) demonstrates the radial velocity $F(\zeta)$ depreciates when the inertia coefficient (Fr) climbs progressively. It is obvious from this figure that an escalation in the inertia coefficient (Fr) leads to the generation of a resistive force on fluid

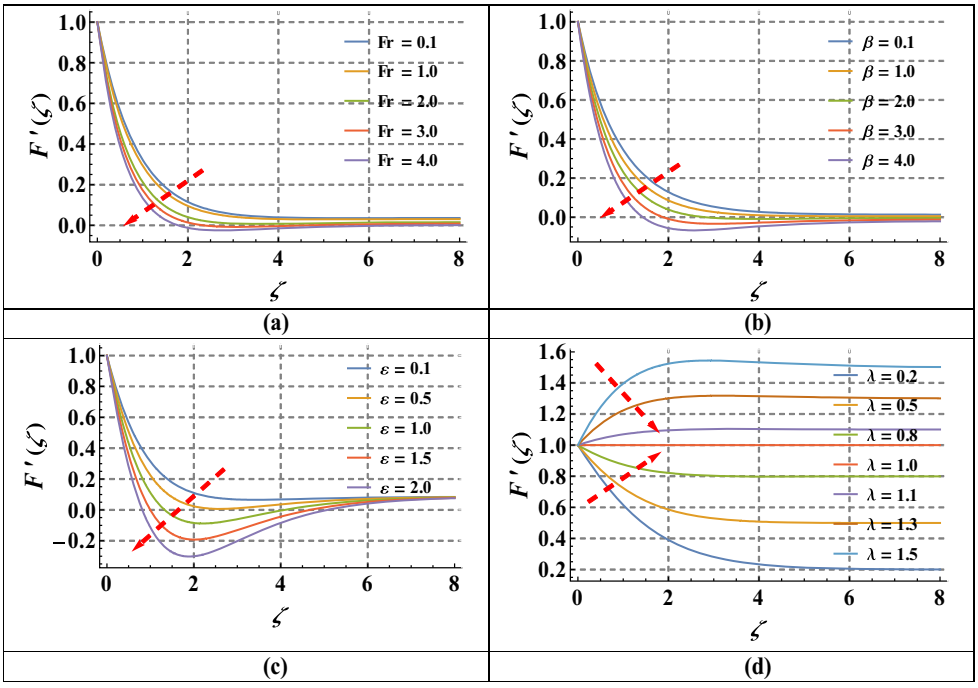

Figure 5: (a) Fluctuation of $F'(\zeta)$ *versus* Fr. (b) Fluctuation of $F'(\zeta)$ *versus* β. (c) Fluctuation of $F'(\zeta)$ *versus* ε. (d) Fluctuation of $F'(\zeta)$ *versus* λ.

motion, which in turn results in a decrease in the flow profile. The role of the porosity variable (β) through the radial velocity $F(\zeta)$ is shown in Figure 5(b). The porosity acts as a decelerating agent that reduces the radial velocity $F(\zeta)$. The obstruction in the liquid flow is produced by the occurrence of porous space, which consequences in a reduction in the speed of fluid. Figure 5(c) depicts the Deborah number (ε) effect on the radial velocity $F(\zeta)$.

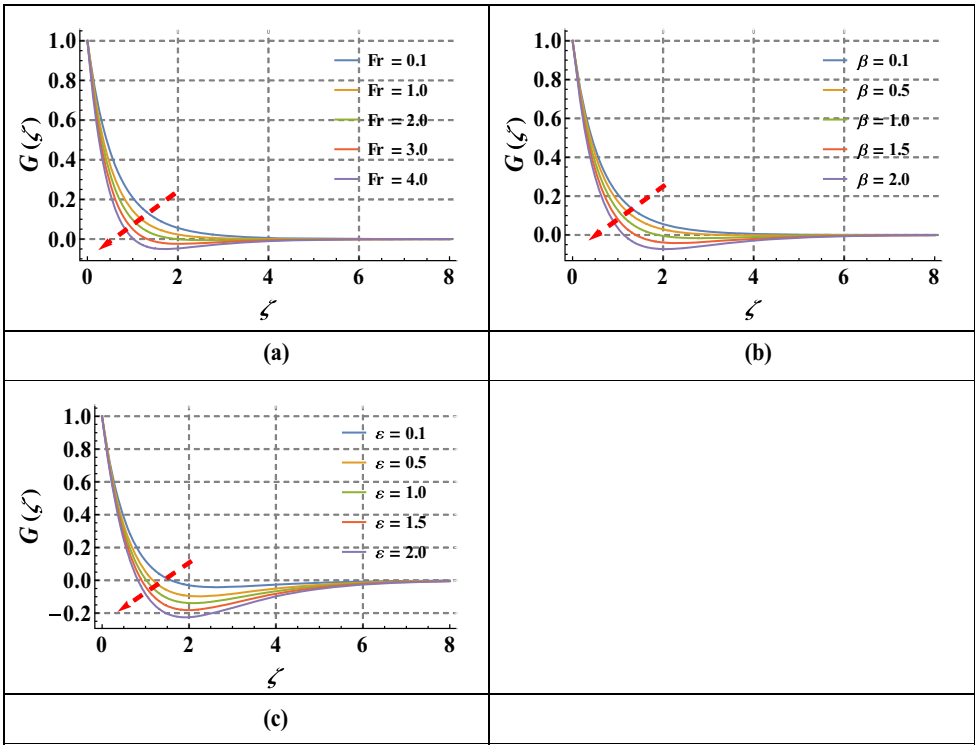

Figure 6: (a) Fluctuation of $G(\zeta)$ *versus* Fr. (b) Fluctuation of $G(\zeta)$ *versus* β. (c) Fluctuation of $G(\zeta)$ *versus* ε.

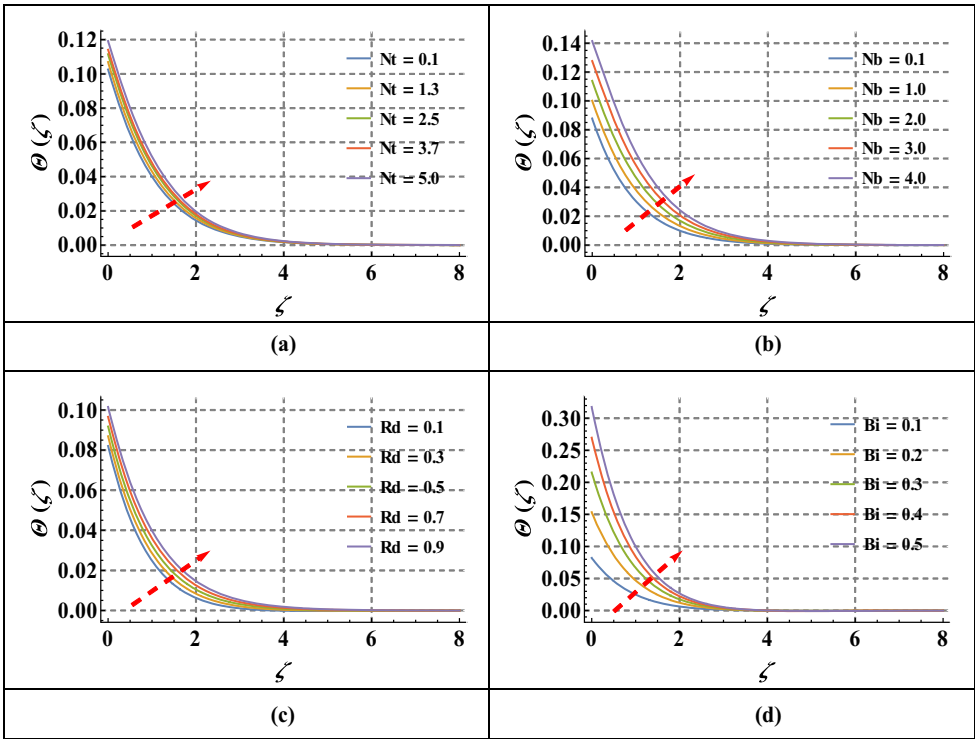

Figure 7: (a) Fluctuation of $\Theta(\zeta)$ *versus* Nt. (b) Fluctuation of $\Theta(\zeta)$ *versus* Nb. (c) Fluctuation of $\Theta(\zeta)$ *versus* Rd. (d) Fluctuation of $\Theta(\zeta)$ *versus* Bi.

A larger magnitude of Deborah's number (ε) causes a visible depreciation for the radial velocity $F(\zeta)$. With a greater amount of the Deborah number (ε), we observe an extended relaxing time in the Maxwell fluid. As a result, the material becomes less fluid and takes on the characteristics of a more solid material. Figure 5(d) displays that as

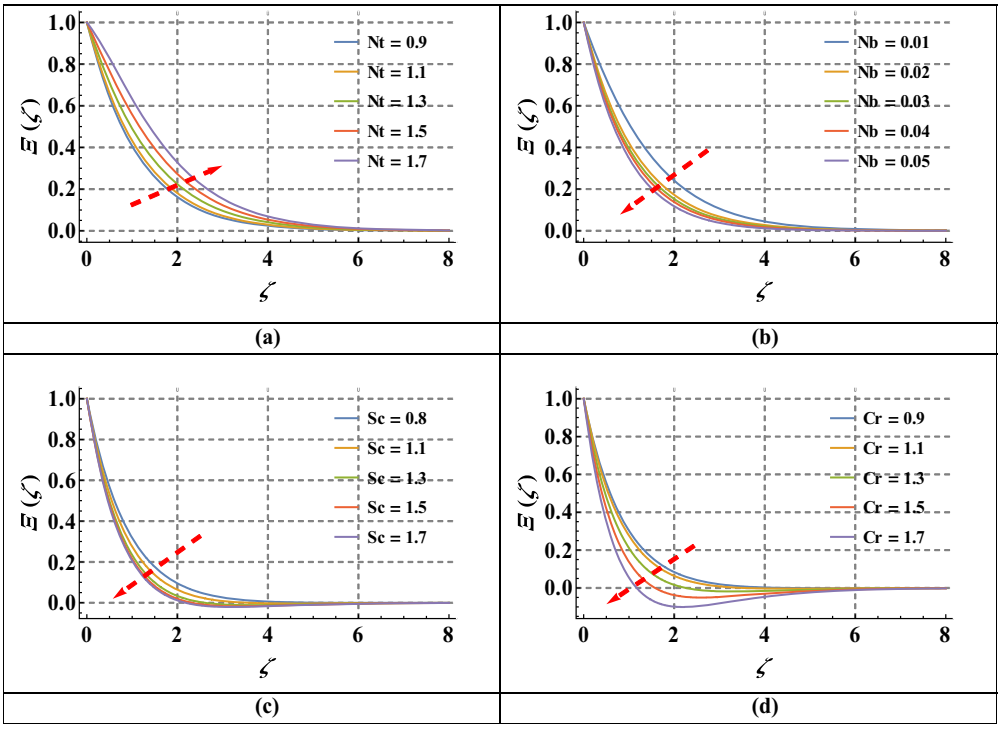

Figure 8: (a) Fluctuation of $\Xi(\zeta)$ *versus* Nt. (b) Fluctuation of $\Xi(\zeta)$ *versus* Nb. (c) Fluctuation of $\Xi(\zeta)$ *versus* Sc. (d) Fluctuation of $\Xi(\zeta)$ *versus* Cr.

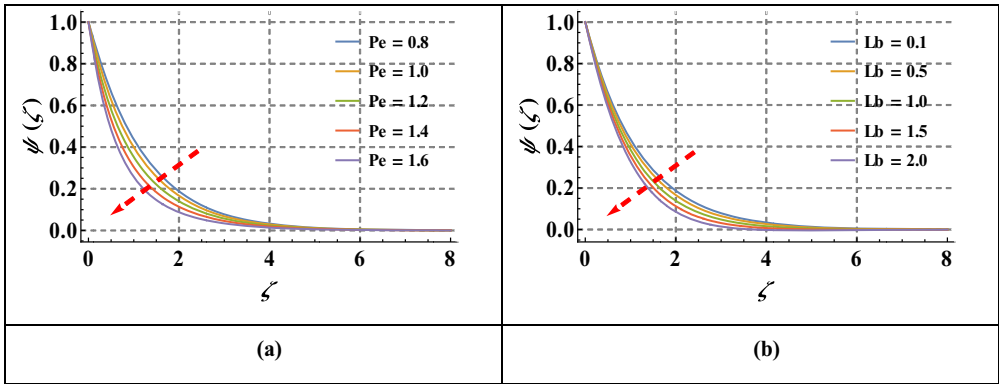

Figure 9: (a) Fluctuation of $\psi(\zeta)$ *versus* Pe. (b) Fluctuation of $\psi(\zeta)$ *versus* Lb.

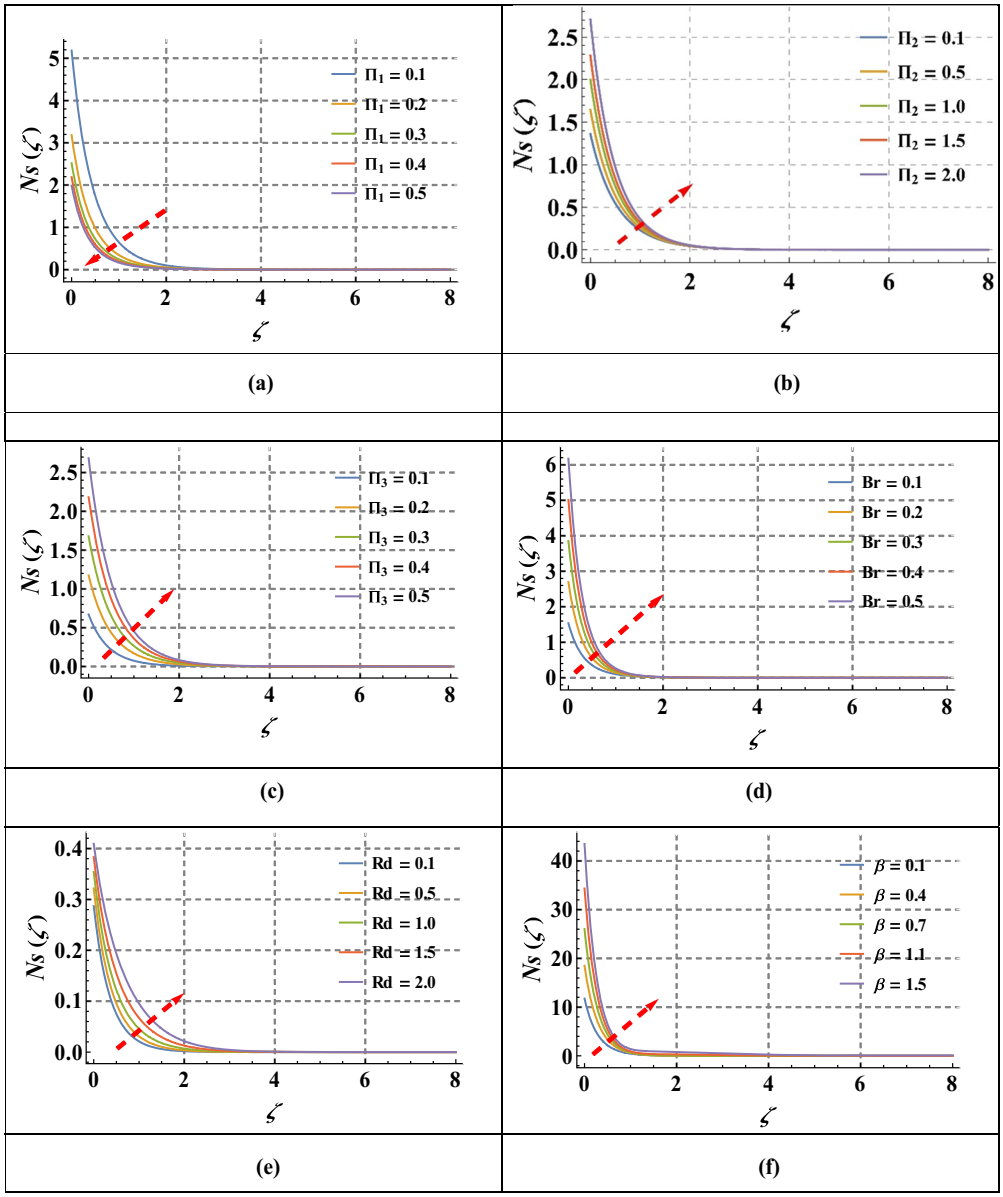

Figure 10: (a) Fluctuation of Ns(ζ) *versus* Π_1. (b) Fluctuation of Ns(ζ) *versus* Π_2. (c) Fluctuation of Ns(ζ) *versus* Π_3. (d) Fluctuation of Ns(ζ) *versus* Br. (e) Fluctuation of Ns(ζ) *versus* Rd. (f) Fluctuation of Ns(ζ) *versus* β.

the velocity ratio (λ) enhances, radial velocity $F(\zeta)$ strongly escalates, meaning the flow accelerates. The stream velocity surpasses the stretching linear velocity as the velocity ratio ($\lambda > 1$). Through an outside flow, it generates a momentum boost that shows up as a high acceleration at all transverse coordinate values, ζ. As a result, the thickness of the velocity is diminished. But when ($\lambda < 1$), the expanding velocity is greater than the velocity free stream, and the reverse effect is considered, meaning that the thickness of the boundary layer grows and the velocity $F(\zeta)$ is suppressed. Both external and stretched velocities are equal when $\lambda = 1$, and this scenario logically lies between $\lambda > 1$ and $\lambda < 1$. It is evident that while a higher external velocity aids in the creation of momentum, a greater stretch of the sheet inhibits it. For $\lambda < 1$ and $\lambda > 1$, a reflection symmetry is calculated about the line $\lambda = 0$. Figure 6(a)–(c) elucidates the effect of the inertia coefficient (Fr), porosity variable (β), and Deborah number (ε) across the azimuthal velocity $G(\zeta)$. A decrease in azimuthal velocity $G(\zeta)$ is associated with a greater estimate of the inertia coefficient (Fr), which is shown in Figure 6(a). Figure 6(b) shows the porosity variable (β) over azimuthal velocity $G(\zeta)$. The azimuthal velocity $G(\zeta)$ decays with the larger magnitude of the porosity variable (β). The azimuthal velocity $G(\zeta)$ through the impact of Deborah number (ε) is visualized in Figure 6(c). The azimuthal velocity $G(\zeta)$ is a declining role of the Deborah number (ε).

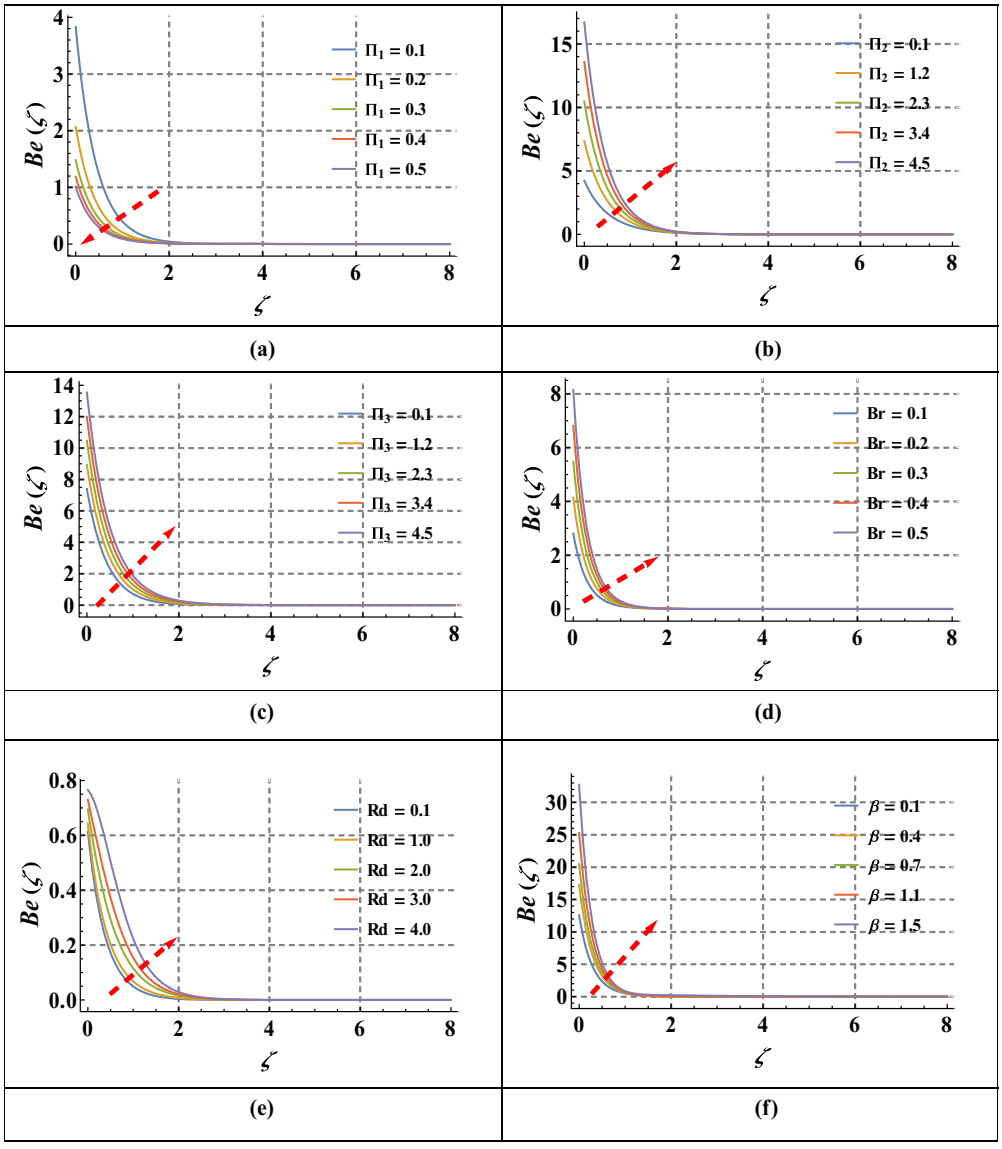

Figure 11: (a) Fluctuation of Be(ζ) *versus* Π_1. (b) Fluctuation of Be(ζ) *versus* Π_2. (c) Fluctuation of Be(ζ) *versus* Π_3. (d) Fluctuation of Be(ζ) *versus* Br. (e) Fluctuation of Be(ζ) *versus* Rd. (f) Fluctuation of Be(ζ) *versus* β.

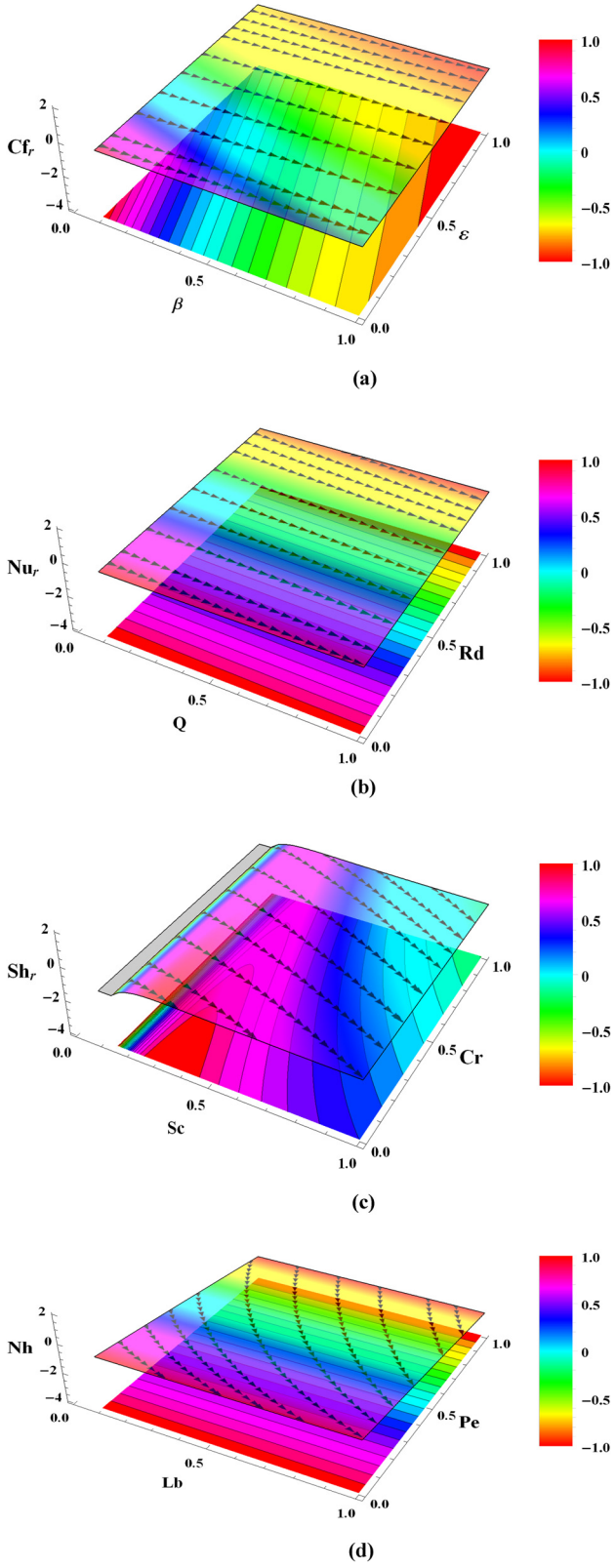

Figure 12: (a) Plot of Cf_r against ε, β. (b) Plot of $\mathrm{Nu_r}$ against Q, Rd. (c) Plot of $\mathrm{Sh_r}$ against Sc, Cr. (d) Plot of Nh against Pe, Lb.

The influence of thermal distribution $\boldsymbol{\Theta}(\zeta)$ with varying thermophoretic force (Nt), Brownian motion (Nb), radiative flow (Rd), and the Biot number (Bi) was shown in Figure 7(a)–(d). Figure 7(a) displays the thermal distribution $\boldsymbol{\Theta}(\zeta)$ *versus* thermophoretic force (Nt). The heat transport escalates the larger estimation of thermophoretic force (Nt). Physically, a rate of heat by a larger thermophoretic body force induces a greater movement of nanoscale particles approaching cooler regions. It additionally raises the heat transfer across the boundary-layer thickness by heating the boundary layer and aggravating thermodiffusion in the regime. Figure 7(b) elucidates the role of Brownian motion (Nb) through the thermal distribution $\boldsymbol{\Theta}(\zeta)$. Greater estimation of Brownian motion (Nb) enhanced the temperature field. A larger estimation of Brownian motion (Nb) results in an enhancement in the rate of diffusion that results in a crash between the fluid of nanoparticles. Figure 7(c) plots the larger values of the radiative variable (Rd) against thermal distribution $\boldsymbol{\Theta}(\zeta)$. An escalation in radiation results in a reduction in the means of absorption, which in turn elevates the thermal layer. Figure 7(d) is designed to illustrate the consequence of the Biot number (Bi) on the thermal field $\boldsymbol{\Theta}(\zeta)$. In the thermally straightforward case, it is noted that the thermal distribution $\boldsymbol{\Theta}(\zeta)$ grows as the Biot number (Bi) increases. Higher values of the Biot number (Bi) indicate an increase in the convection coefficient and a diminution in the rate of heat at the body's surface. Consequently, the fluid receives a greater amount of heat from the rotating surface.

Figure 8(a)–(d) develops the phenomena of thermophoresis number (Nt), Brownian motion (Nb), Schmidt number (Sc), and the chemical reaction (Cr) against concentration distributions $\Xi(\zeta)$. Figure 8(a) is plotted to demonstrate the properties of thermophoresis number (Nt) through the concentration distributions $\Xi(\vartheta)$. Clearly, concentration distributions $\Xi(\vartheta)$ intensified with a larger magnitude of the thermophoresis number (Nt). Physically, a more uniform dispersion of the nanoscale and a greater concentration value are the outcomes of the enhanced movement of the nanoscale over a thermophoretic body force. As shown in Figure 8(b), the value of the concentration field goes down as the value of Brownian motion (Nb) goes up. Brownian motion causes more ballistic collisions, reducing nanoparticle mobility. The role of the Schmidt number (Sc) across the concentration distributions $\Xi(\zeta)$ is shown in Figure 8(c). The mounting magnitude of the Schmidt number (Sc) rises to decrease the concentration distributions $\Xi(\zeta)$. The Schmidt number (Sc) is the rate of diffusion coefficient, resulting in depreciation in concentration distributions $\Xi(\vartheta)$. Figure 8(d) sketches the effect of

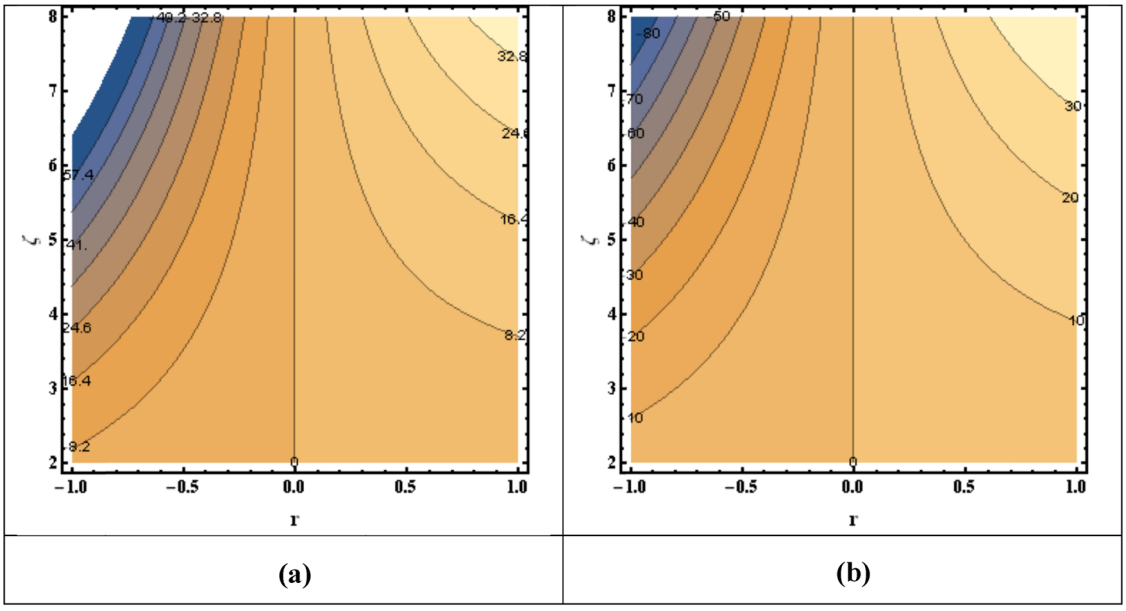

Figure 13: (a) Contour plot for the $A = 0.1$, $\beta = 0.1$. (b) Contour plot for the $A = 0.1$, $\beta = 0.1$.

chemical reaction (Cr) on the concentration distributions $\Xi(\zeta)$. The concentration distribution $\Xi(\zeta)$ declines as the chemical distribution reaction (Cr) changes. The motile density $\psi(\zeta)$ reduces with the enhancing magnitude of (Pe) and (Lb) as shown in Figure 9a and b, respectively. As the two parameters grow, the characteristic of $\psi(\zeta)$ diminishes. The Peclet number (Pe) stimulates the swimming of self-moving microorganisms in the fluid, reducing the number of motile densities $\psi(\zeta)$ moving near the plate. When the bioconvection Lewis number (Lb) rises, the diffusivity of bacteria decreases. This means fewer bacteria are moving. As the motile density $\psi(\zeta)$ grows, the thickness of the boundary layer decreases as well.

Figure 10(a)–(f) observes the entropy production $\mathrm{Ns}(\zeta)$ against the different values of temperature difference variable (Π_1), concentration difference variable (Π_2),

Table 4: Computational value $Cf_r \mathrm{Re}_r^{1/2}$ of ε, γ, Fr, λ

Fr	ε	γ	λ	$Cf_r \mathrm{Re}_r^{1/2}$
0.1	0.1	0.3	0.4	0.543448
0.5				0.586655
1.0				0.638578
1.5				0.688375
	0.1			0.523830
	0.5			0.601999
	1.0			0.698185
	1.5			0.792141
		0.3		0.491870
		0.8		0.639901
		1.0		0.905861
		1.5		2.249380
			0.6	1.035040
			0.9	1.590170
			1.3	2.453310
			1.7	3.662351

Table 5: Computational value $\mathrm{Nu}_r \mathrm{Re}_r^{-1/2}$ of Bi, Rd, Pr, Q and Nb

Q	Bi	Nb	Rd	Pr	$\mathrm{Nu}_r \mathrm{Re}_r^{-1/2}$ HAM
0.1	0.1	0.2	0.5	0.5	0.182637
2.0					0.201852
4.0					0.214308
5.0					0.225998
	0.1				0.102529
	0.2				0.186461
	0.3				0.255664
	0.4				0.313208
		0.1			0.191433
		0.2			0.186461
		0.3			0.187079
		0.4			0.174480
			0.1		0.554620
			0.8		0.539912
			1.4		0.528841
			1.8		0.521517
				0.7	0.282323
				1.0	0.290626
				1.3	0.294336
				1.6	0.299980

Table 6: Computational value $Sh_r Re_r^{-1/2}$ of Nb, Nt, Sc and Kr

Nb	Sc	Nt	Cr	$Sh_r Re_r^{\frac{1}{2}}$ HAM
0.1	0.5	1.0	1.1	1.082730
1.0				1.086250
2.0				1.086942
3.0				1.087571
	0.8			0.825642
	1.2			1.220841
	1.5			1.422021
	1.8			1.699320
		0.2		0.641201
		0.4		0.644157
		0.6		0.646998
		0.8		0.653262
			1.3	0.581811
			1.5	0.678084
			1.7	0.734808
			1.9	0.820668

microorganism difference variable (Π_3), Brinkman number (Br), thermal radiation (Rd), and porosity variable (β). Figure 10(a) confirms the role of temperature difference variable (Π_1) entropy production Ns(ζ). The entropy production Ns(ζ) reduces as the larger magnitude of the temperature difference variable (Π_1). Physically, as the temperature difference variable (Π_1) rises, so does the erratic behavior of the molecules, increasing the system's entropy. Figure 10(b) exemplifies when the concentration difference variable (Π_2) affects the entropy production Ns(ζ). The sketch displays the enhancement in the entropy production Ns(ζ) for the mounting magnitude of the concentration difference variable (Π_2). In fact, the lesser the concentration, the higher the entropy, and consequently, the lower the free energy. Figure 10(c) views the outcomes of entropy production Ns(ζ) for the microorganism difference variable (Π_3). This variable boosts entropy production Ns(ζ) that impacts the movement of included molecules to the flow near the disk. Figure 10(d) visualizes the entropy production Ns(ζ) for the various ascending magnitude of the Brinkman number (Br). A greater Brinkman number improves the viscoelastic force and therefore raises the potential of fluid particles colliding. Due to this entropy production, Ns(ζ) increased. Figure 10(e) and (f) displays that the thermal radiation (Rd) and porosity variable (β) influence the entropy production Ns(ζ). Higher magnitudes of the thermal radiation (Rd) and porosity variable (β) causes an increment in entropy production Ns(ζ).

Table 7: Computational value $Nh_r Re_r^{-1/2}$ of Lb, Pe and ϖ

Lb	ϖ	Pe	HAM $Nh Re_r^{\frac{1}{2}}$
0.1	1.2	1.0	0.622188
0.3			0.684480
0.6			0.722514
0.8			0.781558
	0.3		0.607557
	0.5		0.630634
	0.9		0.642544
	1.1		0.668622
		1.0	0.731177
		1.2	1.128110
		1.3	1.403690
		1.6	1.878517

Figure 11(a)–(f) witnesses the Bejan number Be(ζ) for the various magnitude of the temperature difference variable (Π_1), concentration difference variable (Π_2), microorganism difference variable (Π_3), Brinkman number (Br), thermal radiation (Rd), and porosity variable (β). Figure 11(a) depicts the Bejan number Be(ζ) behavior in relation to the temperature difference variable (Π_1). Greater estimation of the temperature difference variable depreciates the Bejan number. Figure 11(c) shows the features of microorganism difference variable (Π_3) on the Bejan number Be(ζ). Here, the Bejan number Be(ζ) boosts *via* bigger microorganism difference variable (Π_3). Figure 11(d) expresses the Bejan number Be(ζ) due to the larger values of Brinkman number (Br). The Brinkman number is the heat transmitted *via* molecular conduction near the disk, which transfers more heat. The silent feature of the thermal radiation (Rd) and porosity variable (β) on the Bejan number Be(ζ) is shown in Figure 11(e)–(f). The Bejan number Be(ζ) intensifies for the thermal radiation (Rd) and porosity variable (β).

Figure 12(a) illustrates the effect of ε and β on Cf_r. Cf_r reduces with the larger values of the ε and Cf_r enhances the growth of β. Figure 12(b) exhibits the consequences of Rd and Q over Nu_r. It is evident that the escalating the Rd heat transport is enhanced that describe the thickness of boundary. The heat transport on the disk is reduced due to the mounting magnitude of Q. The mass transfer rate Sh_r is altered by the Schmidt number (Sc) and the chemical reaction (Cr) as shown in Figure 12(c). The value of Sh_r decreases gradually as the Schmidt number (Sc) and the chemical reaction (Cr) increase. Figure 12(d) demonstrates the effect of Nh_r with bioconvection Lewis on the microbial density (Lb) and the Peclet number (Pe). Figure 13(a) and (b) elaborates the contour plot for magnetic field (M), inertia coefficient (Fr), porosity variable (β), and fluid variable (γ).

Table 4 presents the numeric evaluation of the $Cf_r Re_r^{1/2}$ for inertia coefficient (Fr), porosity variable (β), Deborah number (ε), and rotating variable (γ). The skin friction coefficient goes up as the nertia coefficient (Fr), porosity variable (β), Deborah number (ε), and rotating variable (γ). Table 5 displays the heat rates depreciation with a higher magnitude of Brownian movement (Nb) and thermal radiation (Rd) but accelerates for heat source-sink parameter (Q), Prandl number (Pr), and Biot number (Bi). As shown in Table 6, higher values of Brownian motion (Nb), chemical reaction parameter (Cr), Schmidt number (Sc), and thermophoresis parameter (Nt) lead to a greater mass concentration gradient. Table 7 indicates the Peclet number (Pe), Bioconvection Lewis number (Lb), and microorganism difference variable (ϖ) make the motile number rise more quickly.

8 Final remarks

The purpose of this work is to examine the axisymmetric flow of a second law analysis on Maxwell bio-nanofluid with the Darcy Forchheimer flow, which is induced by a spinning disk. Radiative and chemical reactive are employed to describe the heat and mass transport phenomena when nanoparticles are present in the fluid. The von Kármán transformations are employed to convert PDEs into ODEs. Analytically and numerically, solutions are applied to modeled equations. Ultimately, the following significant outcomes are provided.

- The depreciation is noted for the radial velocity $F'(\zeta)$ and azimuthal velocity is noted through inertia coefficient (Fr) and Deborah number (ε).
- The residual error and convergence have been produced for the difference order.
- The temperature distribution $\Theta(\zeta)$ grows as Biot number (Bi) and thermal radiation variable (Rd).
- The temperature $\Theta(\zeta)$ and concentration distributions $\Xi(\zeta)$ are enhanced as a result of an increase in the thermophoresis parameter (Nt).
- Concentration profile $\Xi(\zeta)$ is reduced with larger values of the Scimdth number (Sc) and chemical reaction variable (Cr).
- Varying the Brikmann number (Br), concentration difference variable (Π_2), and concentration difference variable (Π_2) develops the entropy production $\mathrm{Ns}(\zeta)$ and Bejan number $\mathrm{Be}(\zeta)$.
- The entropy production $\mathrm{Ns}(\zeta)$ and Bejan number $\mathrm{Be}(\zeta)$ tends to reduce for the larger values of temperature difference variable (Π_1).

Acknowledgments: The authors extend their appreciation for the support received from Princess Nourah bint Abdulrahman University Researchers Supporting Project number (PNURSP2025R163), Princess Nourah bint Abdulrahman University, Riyadh, Saudi Arabia.

Funding information: Princess Nourah bint Abdulrahman University Researchers Supporting Project number (PNURSP2025R163), Princess Nourah bint Abdulrahman University, Riyadh, Saudi Arabia.

Author contributions: F.A. and M.F.A.: conceptualization, methodology, software, formal analysis, validation, and writing – original draft. A.Z. and S.S.Z: writing – original draft, data curation, investigation, visualization, and validation. U.K: conceptualization, writing – original draft, writing – review and editing, supervision, and resources. S.E.: validation, writing – review and editing, software, conceptualization, project administration, funding acquisition, and provided significant feedback and assisted in the revised version of the manuscript. Further, she has also supported in revising the manuscript critically for important intellectual content. All authors have accepted responsibility for the entire content of this manuscript and approved its submission.

Conflict of interest: The authors state no conflict of interest.

Data availability statement: The datasets generated and/or analyzed during the current study are available from the corresponding author on reasonable request.

References

[1] Maxwell JC. IV. On the dynamical theory of gases. Philos Trans R Soc Lond. 1867;157:49–88.
[2] Jawad M, Saeed A, Gul T, Shah Z, Kumam P. Unsteady thermal Maxwell power law nanofluid flow subject to forced thermal Marangoni Convection. Sci Rep. 2021;11:7521.
[3] Ali R, Asjad MI, Aldalbahi A, Rahimi-Gorji M, Rahaman M. Convective flow of a Maxwell hybrid nanofluid due to pressure gradient in a channel. J Therm Anal Calorim. 2020;143:1319–29.
[4] Parvin S, Isa SSPM, Duais FSA-, Hussain SM, Jamshed W, Safdar R, et al. The flow, thermal and mass properties of Soret-Dufour model of magnetized Maxwell nanofluid flow over a shrinkage inclined surface. PLoS One. 2022;17:e0267148.
[5] Safdar R, Jawad M, Hussain S, Imran M, Akgül A, Jamshed W. Thermal radiative mixed convection flow of MHD Maxwell

nanofluid: Implementation of buongiorno's model. Chin J Phys. 2021;77:1465–78.
[6] Algehyne EA, El-Zahar ER, Elhag SH, Bayones FS, Nazir U, Sohail M, et al. Investigation of thermal performance of Maxwell hybrid nanofluid boundary value problem in vertical porous surface *via* finite element approach. Sci Rep. 2022;12:2335.
[7] Khan Z, Zuhra S, Islam S, Raja MAZ, Ali A. Modeling and simulation of Maxwell nanofluid flows in the presence of Lorentz and Darcy–Forchheimer forces: toward a new approach on Buongiorno's model using artificial neural network (ANN). Eur Phys J Plus. 2023;138:107.
[8] Jameel M, Shah Z, Rooman M, Alshehri MH, Vrinceanu N. Entropy generation analysis on Darcy-Forchheimer Maxwell nanofluid flow past a porous stretching sheet with threshold Non-Fourier heat flux model and Joule heating. Case Stud Therm Eng. 2023;52:103738.
[9] Wang F, Awais M, Parveen R, Alam MK, Rehman S, Deif AMH, et al. Melting rheology of three-dimensional Maxwell nanofluid (graphene-engine-oil) flow with slip condition past a stretching surface through Darcy-Forchheimer medium. Results Phys. 2023;51:106647.
[10] Zeng S, Liu J, Ma C. Topology optimization in cooling moving heat sources for enhanced precision of machine tool feed drive systems. Int J Therm Sci. 2024;202:109065.
[11] Han T, Zhang S, Zhang C. Unlocking the secrets behind liquid superlubricity: A state-of-the-art review on phenomena and mechanisms. Friction. 2024;10(8):1137–65.
[12] Choi SUS, Estman J. Enhancing thermal conductivity of fluids with nanoparticles. ASME-Publications-Fed. 2001;231:718–20.
[13] Buongiorno J. Convective transport in nanofluids. J Heat Transf. 2005;128:240–50.
[14] Waqas M, Khan MI, Hayat T, Gulzar MM, Alsaedi A. Transportation of radiative energy in viscoelastic nanofuid considering buoyancy forces and convective conditions. Chaos Solitons Fractals. 2020;130:109415. doi: 10.1016/j.chaos.2019.109415.
[15] Anjum N, Khan WA, Hobiny A, Azam M, Waqas M, Irfan M. Numerical analysis for thermal performance of modified Eyring Powell nanofluid flow subject to activation energy and bioconvection dynamic. Case Studies Therm Eng. 2022;39:102427. doi: 10.1016/j.csite.2022.102427.
[16] Mabood F, Shamshuddin Md, Mishra SR. Characteristics of thermophoresis and Brownian motion on radiative reactive micropolar fluid flow towards continuously moving flat plate: HAM solution. Math Computers Simul. 2021;191:187–202.
[17] Ahmad S, Hayat T, Alsaedi A. Numerical analysis of entropy generation in viscous nanofluid stretched flow. Int Commun Heat Mass Transf. 2020;117:104772.
[18] Shahzad A, Imran M, Tahir M, Khan SA, Akgül A, Abdullaev S, et al. Brownian motion and thermophoretic diffusion impact on Darcy-Forchheimer flow of bioconvective micropolar nanofluid between double disks with Cattaneo-Christov heat flux. Alex Eng J. 2022;62:1–15.
[19] Karthik K, Saadeh R, Kumar RSV, Qazza A, Madhukesh JK, Khan U, et al. Computational analysis of water-based silver, copper, and alumina hybrid nanoparticles over a stretchable sheet embedded in a porous medium with thermophoretic particle deposition effects. Nanotechnol Rev. 2024;13(1):20240083.
[20] Elboughdiri N, Fatima N, Abd El-Rahman M, Abbas M, Rashid RF, Shomurotova S, et al. Characteristics of unsteady thermo-bioconvection, chemical, reactive, stagnation, point flow of trihybrid, nanofluid, around rotating sphere, with oxytactic microorganisms. Case Stud Therm Eng. 2024;61:104981.
[21] Zhou G, Huang J, Li H, Li Y, Jia G, Song N, et al. Multispectral camouflage and radiative cooling using dynamically tunable metasurface. Opt Express. 2024;32(7):12926–40.
[22] Wang H, Hou Y, He Y, Wen C, Giron-Palomares B, Duan Y, et al. A Physical-constrained decomposition method of infrared thermography: Pseudo restored heat flux approach based on Ensemble Bayesian Variance Tensor Fraction. IEEE Trans Ind Inform. 2023;20(3):3413–24.
[23] He J, Hou Q, Yang X, Duan H, Lin L. Isolated slug traveling in a voided line and impacting at an end orifice. Phys Fluids. 2024;36(2):027105.
[24] Rajeswari PM, De P. Shape factor and sensitivity analysis on stagnation point of bioconvective tetra-hybrid nanofluid over porous stretched vertical cylinder. BioNanoScience. 202414:3035–58.
[25] Darcy HPG. Les Fontaines publiques de la ville de Dijon. Exposition et application des principes à suivre et des formules à employer dans les questions de distribution d'eau, etc. Paris: V. Dalamont.; 1856.
[26] Forchheimer P. Wasserbewegung durch boden. Z Ver Deutsch Ing. 1901;45:1782–8.
[27] Muskat M. The flow of homogeneous fluids through porous media. Soil Sci. 1938;46:169.
[28] Sahu SK, Shaw S, Thatoi DN, Azam M, Nayak MK. Darcy-Forchheimer flow behavior and thermal inferences with SWCNT/MWCNT suspensions due to shrinking rotating disk*. Waves in random and complex media; 2022. p. 1–29. doi: 10.1080/17455030.2022.2094496
[29] Nisha SS, De P. Impact of electro-osmotic, activation energy and chemical reaction on Sisko fluid over Darcy–Forchheimer porous stretching cylinder. Proc Inst Mech Eng Part E J Process Mech Eng. 2024.
[30] Ahmad S, Tiamiyu AT. Numerical simulation of time-dependent non-Newtonian compressible fluid flow in porous media: Finite element method and time integration approach. Int Commun Heat Mass Transf. 2024;159:107934.
[31] Shah Z, Sulaiman M, Dawar A, Alshehri MH, Vrinceanu N, Darcy–Forchheimer MHD rotationally symmetric micropolar hybrid-nanofluid flow with melting heat transfer over a radially stretchable porous rotating disk. J Therm Anal Calorim. 2024.
[32] Von Karman T. Uber laminate und turbulent reibung. Z Angew Math Mech. 1921;1:233–52.
[33] Khan M, Ahmed J, Ali W, Nadeem S. Chemically reactive swirling flow of viscoelastic nanofluid due to rotating disk with thermal radiations. Appl Nanosci. 2020;10:5219–32.
[34] Song Y-Q, Khan SA, Imran M, Waqas H, Khan SU, Khan MI, et al. Applications of modified Darcy law and nonlinear thermal radiation in bioconvection flow of micropolar nanofluid over an off centered rotating disk. Alex Eng J. 2021;60:4607–18.
[35] Bu W, Xu H, Khan I, Ullah Khan SI, Zeb A. Mixed convection squeezing flow of nanofluids in a rotatingchannel with thermal radiation. J Math. 2022;15. Article ID 3885463. doi: 10.1155/2022/3885463.
[36] Ahmad S, Hayat T, Alsaedi A, Ullah H, Shah F. Computational modeling and analysis for the effect of magnetic field on rotating stretched disk flow with heat transfer. Propuls Power Res. 2021;10:48–57.
[37] Sharma K, Vijay N, Duraihem FZ, Jindal R. Flow analysis of water conveying nanomaterials over a rotating surface with thermal radiation. Multidiscip Modeling Mater Struct. 2024;20:784–95.

[38] Gomathi N, Poulomi D. Dual solutions of Casson Williamson nanofluid with thermal radiation and chemical reaction. Numer Heat Transf Part a Appl. 2024;86(15):5161–84.
[39] Ahmad S, Hayat T, Alsaedi A. Computational analysis of entropy generation in radiative viscous fluid flow. J Therm Anal Calorim. 2020;143:2665–77.
[40] Owhaib W, Basavarajappa M, Al-Kouz W. Radiation effects on 3D rotating flow of Cu-water nanoliquid with viscous heating and prescribed heat flux using modified Buongiorno model. Sci Rep. 2021;11:1593.
[41] Nadeem S, Ijaz M, Ayub M. Darcy–Forchheimer flow under rotating disk and entropy generation with thermal radiation and heat source/sink. J Therm Anal Calorim. 2020;143:2313–28.
[42] Sharma K. FHD flow and heat transfer over a porous rotatingdisk accounting for Coriolis force along with viscous dissipation and thermal radiation. Heat Transf. 2022;51:4377–92.
[43] Nasir M, Waqas M, Bég OA, Basha DB, Zamri N, Leonard HJ, et al. Chemically reactive Maxwell nanoliquid flow by a stretching surface in the frames of Newtonian heating, nonlinear convection and radiative flux: Nanopolymer flow processing simulation. Nanotechnol Rev. 2022;11:1291–306.
[44] Liao S. Beyond Perturbation: Introduction to the homotopy analysis method. Florida, USA: CRC Press; 2003.
[45] Khan U, Zaib A, Bakar SA, Ishak A. Unsteady stagnation-point flow of a hybrid nanofluid over a spinning disk: analysis of dual solutions. Neural Comput Appl. 2022;34:8193–210.
[46] Liao S. An optimal homotopy-analysis approach for strongly nonlinear differential equations. Commun Nonlinear Sci Numer Simul. 2009;15:2003–16.
[47] Ramesh GK, Gireesha BJ, Hayat T, Alsaedi A. Stagnation point flow of Maxwell fluid towards a permeable surface in the presence of nanoparticles. Alex Eng J. 2016;55:857–65.
[48] Mathew A, Areekara S, Sabu AS, Saleem S. Significance of multiple slip and nanoparticle shape on stagnation point flow of silver-blood nanofluid in the presence of induced magnetic field. Surf Interfaces. 2021;25:101267.